NTNU
Det skapende universitet

Spraypyrolyse av keramiske oksidmaterialer

Roger Moen

Nanoteknologi
Innlevert: juni 2013
Hovedveileder: Mari-Ann Einarsrud, IMTE
Medveileder: Tor Grande, IMT
Ruth Astrid Strøm, Cerpotech

Norges teknisk-naturvitenskapelige universitet
Institutt for materialteknologi

(Dedicated to my coming first child. May your life be filled with joy and happiness.)

Declaration of Independence

I hereby declare that the work in this thesis has been performed independently and in accordance with the examination regulations of Norwegian University of Science and Technology (NTNU).

_____

Roger Moen

Abstract

This thesis is a study of the effect of process and chemical parameters in preparation of ceramic oxides by spray pyrolysis. The investigations have been performed by preparation of europium-doped and undoped yttrium oxide powder, Y_2O_3, in a large-scale preparation unit. Varying one parameter at a time, the effect of each parameter was assessed. The chemical parameter investigated in this work was complexing agents. Non-complexed precursor solution was compared with solutions complexed with ethylenediaminetetraacetic acid or maleic acid. The process parameters studied were the flow rates of carrier gas and precursor solution. The investigated carrier gas flow rates were 15, 30 and 40 $m^3\ h^{-1}$, while the precursor solution flow rates were 75, 150 and 300 mL min^{-1}. The samples prepared with flow rates of carrier gas and precursor solution 30 $m^3\ h^{-1}$ and 75 mL min^{-1}, respectively, were reproduced with 1.5 % europium doping. All samples were calcined at 600 °C for 2 hours and characterized with respect to yield, phase purity, crystallite size, particle size, particle morphology and specific surface area. For the europium-doped samples photoluminescence performance was also characterized. The samples were nanocrystalline, with average crystallite sizes below 20 nm for calcined samples. The particles were mostly spherical, but when complexing agents were used, the fraction of particles with irregular shape increased. This was attributed to internal pressure build-up and lower mechanical strength. It was shown that when the ratio between the flow rates of precursor solution and carrier gas was high, some of the powders were moist. High partial pressure of water vapor with subsequent saturation and condensation was proposed as explanation. The photoluminescence performance was lower for the europoium-doped sample prepared with ethylenediaminetetraacetic acid as complexing agent.

Sammendrag

Denne oppgaven er et studium av effekten av prosessparametere og kjemiske parametere i produksjon av keramiske oksider ved spraypyrolyse. Undersøkelsene har blitt utført ved fremstilling av europiumdopet og ikke-dopet pulver av yttriumoksid, Y_2O_3, i en storskalafremstillingsenhet. Ved å variere én parameter om gangen ble effekten av den enkelte parameter undersøkt. Den kjemiske parameteren som ble undersøkt i dette arbeidet var komplekseringsmiddel. Ikke-komplekserte forløperløsninger ble sammenlignet med løsninger kompleksert med etendiamintetraacetatsyre eller maleinsyre. Prosessparameterne som ble undersøkt var gjennomstrømningshastighet av bæregass og forløperløsning. De undersøkte gjennomstrømningshastighetene var 15, 30 og 40 m^3 per time for bæregass og 75, 150 og 300 mL per minutt for forløperløsning. Prøvene fremstilt med en gjennomstrømning av bæregass på 30 m^3 per time og forløperløsning på 75 mL per minutt ble reprodusert med 1,5 % europiumdoping. Alle prøver ble kalsinert ved 600 °C i 2 timer og karakterisert med hensyn på utbytte, faserenhet, krystallstørrelse, partikkelstørrelse, partikkelmorfologi og spesifikt overflateareal. For de europiumdopede prøvene ble også fotoluminescensegenskaper undersøkt. Prøvene var nanorkrystallinske med gjennomsnittlige krystallstørrelser under 20 nm for kalsinerte prøver. Partiklene var for det meste sfæriske, men når komplekseringsmidler ble brukt, økte andelen av partikler med uregelmessig form. Dette ble tilskrevet intern trykkoppbygning og lavere mekanisk styrke. Det ble vist at når forholdet mellom gjennomstrømningshastigheten til forløperløsning og bæregass var høyt, ble noen av pulverne fuktige. Høyt partialtrykk av vanndamp med påfølgende metning og kondensering ble foreslått som forklaring. Fotoluminescensytelsen var lavere i den europiumdopede prøven som ble fremstilt med etendiamintetraacetatsyre som komplekseringsmiddel.

Preface

This thesis is part of the Master of Science program in nanotechnology at the Norwegian University of Science and Technology. The work has been carried out at the Department of Materials Science and Engineering (DMSE) between January 21st and June 27th 2013. It is a natural continuation of the author's own specialization project from the fall semester of 2012. Professor Mari-Ann Einarsrud has served as supervisor, while Professor Tor Grande and Ruth Astrid Strøm have been co-supervisors.

Many people deserve to be thanked for various reasons. First, and above all, my supervisor Professor Einarsrud is thanked for providing an interesting and highly relevant topic and her invaluable guidance, discussions and tips along the way from start to finish. Next, Professor Grande is thanked for answering many questions during the semester when Professor Einarsrud was away or unavailable. PhD candidate Malin Sletnes has helped with both instrument training and experimental work, and she is acknowledged. PhD candidate Sophie Weber is thanked for her introduction to statistical analysis of experimental data. Head of production at Cerpotech AS, Lars-Petter Bjørkeng, is thanked for help and support during preparation of powder samples.

Working with this thesis has been exciting and educational. In addition, it has boosted my interest and fascination for nanotechnology and materials science.

Table of contents

1 Introduction

1.1 Motivation

Trivalent lanthanide-doped oxides display many desirable optical properties and have attracted interest from researchers and industry for several decades. These materials have been used in a wide range of applications, including fluorescent lighting[1], display panels[2], medical diagnostics[3], scintillators[4] and amplifiers for fiber-optical communication[5]. Electronic transitions give rise to unique luminescent spectra for the different dopants, which are used to obtain different colors in displays (terbium or holmium for green, dysprosium for yellow, thulium for blue and europium for red[6]). One of the most common host materials is yttrium oxide, Y_2O_3. Trivalent yttrium ions, Y^{3+}, have a size very close to that of many trivalent lanthanides and Y_2O_3 also has the same crystal structure as many of the lanthanide oxides in addition to relatively high thermal and mechanical stability. Y_2O_3 is therefore known as one of the best host materials for lanthanide ions[7]. Optical properties are affected by several other factors than chemical composition. Size and morphology of crystallites and particles must also be considered when preparing such materials[8, 9]. Small size is a requirement for high brightness and resolution[1]. Nanomaterials are therefore of particular interest. In addition, the concentration of surface defects should be minimized[10].

One of the most thoroughly investigated material systems is europium-doped yttrium oxide, Y_2O_3:Eu^{3+}. Among its advantages are excellent chemical stability, no hazardous constituents and good color characteristics[11, 12]. This particular material has its strongest emission line at 615 nm[13] and has been used as a red emitting phosphor in flat panel displays[14] (see Fig. 1.1), fluorescent lamps and laser devices. Y_2O_3:Eu^{3+} has been synthesized via many different methods, including solid-state reaction[15], combustion[16], solvothermal synthesis[17], hydrothermal synthesis[18], sol-gel[19] and microemulsion[20]. These methods have yielded particles with various morphologies, like rods[21], flower-like[22, 23], spheres[24], cubes[25] and sheets[26]. Traditionally, solid-state reactions have been the preferred preparation methods. This method offer several advantages, such as large low concentrations of surface defects, high luminescence efficiency and inexpensive, easy processing[12]. However, there are also disadvantages associated with this method,

agglomeration, non-homogeneous distribution of dopant and irregular particle morphology being three of them[12]. Therefore, other preparation methods have also been studied and optimized.

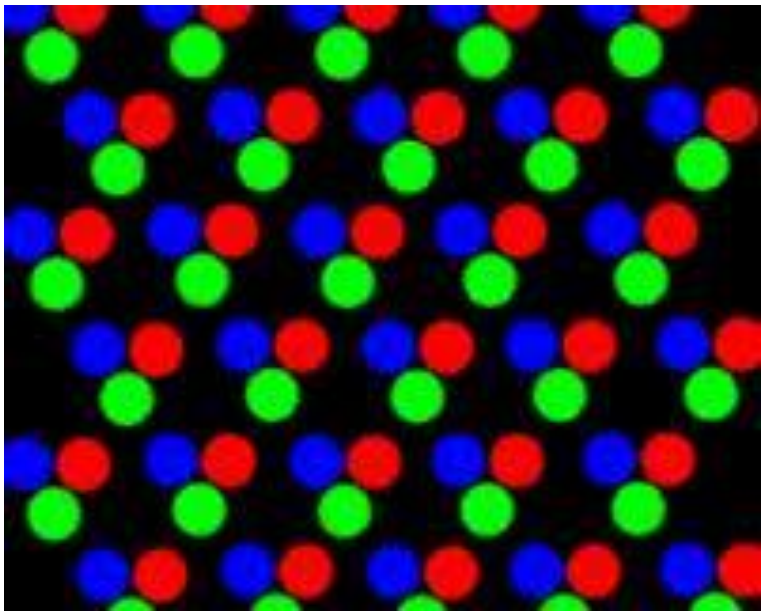

Figure 1.1: *Pixels in a display panel. Each pixel contains three dots with unique colors – red, green and blue. Europium-doped yttrium oxide is commonly used as the red emitter.*

For many decades aerosol processes, such as spray drying, spray pyrolysis and the flame spray method, have been utilized for production of materials in powder form at both laboratory and industrial scale. These methods have been employed for a wide range of materials, including metal oxides[27, 28] , nitrides[29, 30] , carbides[31], borides[32], fullerenes[33] and metals[34, 35]. Over the past decades the interest in spray pyrolysis has increased, as illustrated by the increasing number of publications per year shown in Fig. 1.1. This method yields spherical particles with superior homogeneity and narrow size distribution, and materials for optical applications have shown promising performances[36-38]. Therefore, a large effort has been directed towards optimizing this method for these materials.

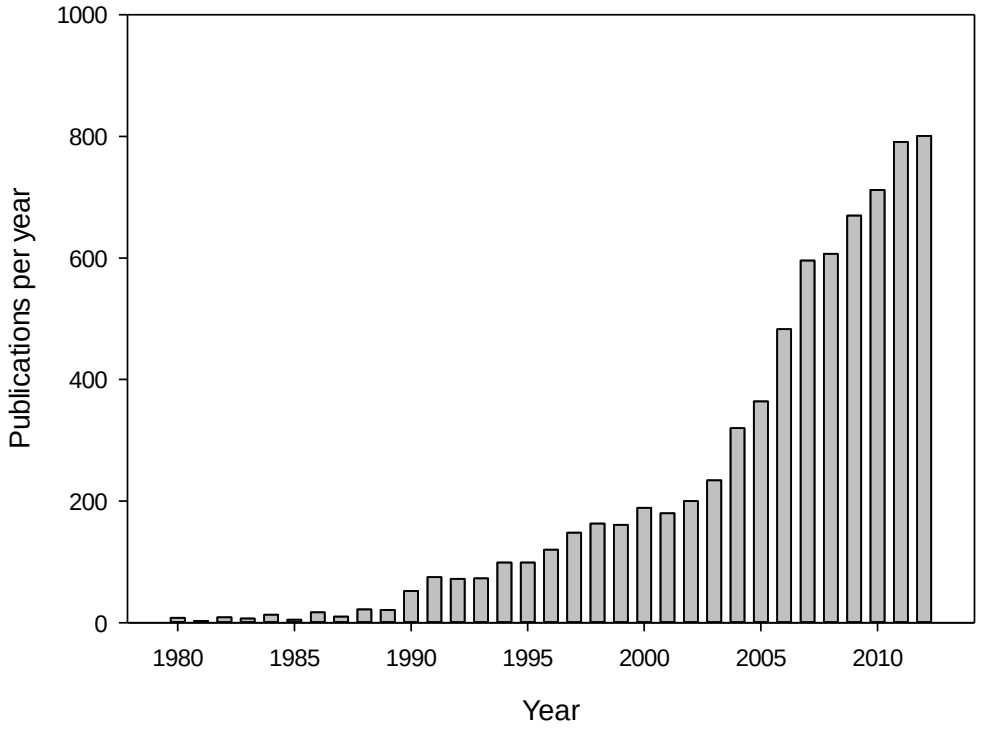

Figure 1.2: *Publications on spray pyrolysis per year between 1980 and 2012. Numbers are taken from the online database Web of Science.*

1.2 Aim of this work

This thesis has aimed at investigating and explaining the effect of process and chemical parameters for preparation of Y_2O_3 and Y_2O_3:Eu^{3+} by spray pyrolysis. The investigated parameters are carrier gas flow, precursor solution feeding rate and complexing agent. This work is a continuation of the author's specialization project[39] carried out during the fall semester 2012. Together these works should form a thorough overview of spray pyrolysis and the effect of the most important parameters. The overall goal has been to obtain defect-free Y_2O_3 and Y_2O_3:Eu^{3+} powder with high chemical purity, high crystallinity and small crystallite size. Other factors such as morphology and surface area should also be examined. For characterization, common techniques including x-ray diffractometry, scanning electron microscopy, gas adsorption, photoluminescence measurements and infrared spectroscopy will be employed.

2 Background

2.1 Spray Pyrolysis

Spray pyrolysis is an aerosol technique used to synthesize many different materials, including metals, metal oxides, semiconductors and more novel materials like fullerenes and superconductors. Spray pyrolysis is traditionally divided into three distinct steps. Each of these steps is important for the characteristics of the product and all are discussed below.

Step I: Atomization of precursor solution. The first step of the spray pyrolysis process is atomization of the precursor solution. The precursor solution is subjected to a force large enough to overcome the surface tension of the solution. This step is important for many parameters of the production process, such as production rate, particle size and particles size distribution. Many techniques are developed for atomization of liquids. In spray pyrolysis the most common is using a nozzle, which is either ultrasonic, electrostatic or uses a second fluid, a so-called two-fluid nozzle. Although their purpose is the same, many properties of the sprays differ between the atomizers used. Characteristics such as droplet velocity, minimum and maximum throughput, droplet size and droplet size distribution are unique to the type of atomizer. In addition to the atomizer itself, also properties of the precursor solution are important. Some important properties of the precursor solution are viscosity, surface tension and density. Table 2.1 (reprinted from Messing *et al.*[40]) compares some characteristics of the most common atomizers.

Step II: Evaporation of the solvent. After atomization, the precursor solution is transported by a carrier gas into a hot-zone where the solvent is removed by evaporation. This step is defined as the period where solvent evaporates from the droplets until all solvent is evaporated. Many physical and chemical processes take place simultaneously during this step: the droplet shrinks, the temperature of the droplet increases, solvent vapor diffuses away from the droplet and the solution concentration increases. Seinfeld[41] defined characteristic time constants for some of the phenomena determining the particle morphology. A characteristic time constant is defined as the time it takes for a process to reach steady state. The ratio between these characteristic time constants can be used to predict the morphology of the

particle.

Step III: Thermolysis and sintering. During this step the precipitated precursor particles thermally decompose to form the product, provided the temperature in the hot-zone is high enough. If the temperature is so low that the precursors do not react, spray pyrolysis is reduced to mere spray drying. The precursors may simply decompose and react to form the product, but can also react with additives in the precursor solution or the carrier gas. If the temperature is high enough to give the particles appreciable mobility, they may sinter and increase their density.

A common challenge with spray pyrolysis is formation of carbonaceous compounds. Sources of carbon can be organic additives in the precursor solution or carbon dioxide in the carrier gas. These compounds often have high thermal and chemical stability. Consequently, a post-preparation thermal treatment is often necessary to obtain a phase pure product.

Table 2.1: *Some typical droplet size and droplet velocity for some common atomizers used in spray pyrolysis.*

Atomizer	Droplet size [µm]
Two-fluid	10 – 100
Ultrasonic	1 – 100
Electrostatic	0.1 – 10

2.2 Phosphors and luminescence

In its most general sense, a phosphor is a material that displays some form of luminescent behavior. Phosphors usually consist of a host material doped with a small amount of an active ion, a so-called activator. The activator is typically a transition metal or a rare-earth ion. Each ion has unique electronic configuration and energetic structure, which gives rise to characteristic absorption and emission spectra. Some common phosphor material systems and their characteristic emission wavelengths are shown in Table 2.2.

Luminescence is defined as the emission of light from a substance due to any other process than heating[42]. Here, light is taken to mean more than light visible to the human eye, and includes also wavelengths outside the visible spectrum. Many different sources of

energy can excite an electron into a higher energetic state. A prefix is often added to indicate what the cause of excitation is. For example, *photo*luminescence and *electro*luminescence indicates that excitation is caused by photons and an electric field, respectively. The emission of light is due to electronic transitions, where an electron is transferred from a high-energy state to a low-energy state. This process is also known as relaxation.

Table 2.2: *Some common phosphor material systems, their respective emission wavelength and the corresponding color.*

Host material	Activator ion	Emission wavelength [nm]	Color
Y_2O_3	Eu^{3+}	615	Red
YVO_4	Eu^{3+}	615	Red
Al_2O_3	Cr^{3+}	693	Red
$La_{0.6}Ce_{0.4}PO_4$	Tb^{3+}	543	Green
$Y_3Al_5O_{12}$	Ce^{3+}	530	Green
ZnS	Cu^{+}	531	Green
ZnS	Ag^{+}	450	Blue
$(Sr,Ba,Ca)_5(PO_4)_3Cl$	Eu^{2+}	450	Blue
Y_2SiO_5	Ce^{3+}	400	Blue

The electronic transitions between atomic energy levels may be classified into two distinct types, phosphorescence and fluorescence. The basis for distinguishing them is well-known principles of quantum mechanics. A short overview of these principles is useful. A single electron can be described by four quantum numbers. The principal quantum number, *n*, gives the main energy level and is related to the size of the electron cloud (shell). It can be any positive integer. The larger the number, the higher is the energy of that particular level. The angular momentum quantum number, ℓ, indicates the sublevels within each main energy level. It can take any integer value between 0 and n - 1. Values of ℓ are usually designated by a letters, where *s*, *p*, *d* and *f* correspond to *l* values of 0, 1, 2 and 3, respectively. The magnetic quantum number, m_ℓ, is given to a specific orbital within the energy sublevels, and describes the spatial orientation of the orbital. m_ℓ takes integer values between $-\ell$ and $+\ell$. Thus, there

are $2\ell+1$ possible values of m_ℓ. The last quantum number is the spin projection number, m_s. It can take only two values, +½ and -½, and represents the spin angular momentum of the electron around its own axis. Often, m_s = +½ and m_s = -½ are referred to as «spin up» and «spin down», respectively. According to the Pauli Exclusion Principle, no two electrons can have identical sets of quantum numbers.

Electrons in incompletely filled orbitals can arrange themselves in several ways. Due to Coulombic interactions, the sublevels are split into energetically different states called *terms*. These terms are described by two numbers. The first number, L, is the total orbital angular momentum. It is given by

$$L = \ell_1 + \ell_2 + \cdots \quad (1)$$

where the subscripts 1, 2, … refers to the individual electrons. Usually, instead of using the number, L is replaced with a capital letter. The relation between the L number and the letter is shown in Table 2.3. The second number, S, is the total spin number. It is given by

$$S = m_{s,1} + m_{s,2} + \cdots \quad (2)$$

where the subscripts are used the same way as in Eq. 1. Combining L and S yields the term symbol, $^{2S+1}L_J$, where 2S+1 is the multiplicity of the term and J is the total angular momentum. Permitted values of J are L+S, L+S-1, L+S-2, … , |L-S|. The $^7F_2$ term may serve as an example: The superscript means the multiplicity is 7, and thus the total spin number S is (7-1)/2=3. F means L=3 and the subscript means the total angular momentum is 2.

Table 2.3: Relation between L and term letters.

L	0	1	2	3	4	…
Term letter	S	P	D	F	G	(Continues in alphabetical order, omitting J)

The emission of light from a phosphor is caused by electronic transitions. First, energy must be absorbed by the host material and then transferred to the activator ion where an electron is excited to a higher energetic state. Through relaxation the excited electron loses energy as it falls back to its original state. The energy difference between these states may be released partly or wholly by emission of electromagnetic radiation, i.e a photon, or a lattice

vibration, i.e. a phonon. Emission of photons and phonons are often referred to as radiative and non-radiative emission, respectively. For optical applications, non-radiative transitions are generally unwanted.

Luminescence may be further classified depending on whether the electron transition is allowed or forbidden. Different types of transitions have their own selection rules. Electric dipole allowed transitions have selection rules $\Delta J = -2, 0, +2$. Selection rules for magnetic dipole transitions are $\Delta J = -1, 0$ or $+1$ (but $J = 0 \rightarrow J = 0$ is forbidden). Emission after a spin forbidden transition is called phosphorescence, and the process usually takes place within nanoseconds. Emission following a spin allowed transition is called fluorescence, and is usually a much slower process that can take between seconds and hours.

Yttrium oxide, Y_2O_3 (also known as yttria), is known as one of the best hosts for rare-earth ions due to its similarity in both ionic radius and crystal structure[7]. Europium-doped yttria, $Y_2O_3:Eu^{3+}$, is among the most thoroughly studied and commercially popular red-emitting phosphors. Elemental europium has the electronic configuration $[Xe]4f^76s^2$. For many rare-earths, the 4f electrons are spatially located closer to the nucleus than are the 5s and 5p electrons, despite being higher in energy. Therefore the 4f electrons are shielded by the 5s and 5p electrons and contribute very little to the chemical properties of these elements[43]. Europium forms no exception from this trend. Trivalent europium, Eu^{3+}, has electronic configuration $[Xe]4f^6$. Among the many possible electronic transitions of this ion, the strongest emission is due to the electric dipole allowed $^5D_0 \rightarrow {}^7F_2$ transition. The energy difference between these states is approximately 16 260 cm^{-1} (2.016 eV), corresponding to a wavelength of 615 nm giving red light Europium ions can occupy two unique sites in the Y_2O_3 lattice. These are shown schematically in Fig. 2.1 (reprinted from Ref. [44]). One site is centrosymmetric, and the other is non-centrosymmetric. Both sites are located at the center of a cube, where six of the corners are occupied by O^{2-} anions, and the two other corners are vacant. At the centrosymmetric site, S_6, the vacancies are located at the body diagonal, whereas for the non-centrosymmetric site, C_2, they are located at the face diagonal. The C_2 sites are three times more abundant than the S_6 site in the Y_2O_3 lattice. Transitions from the C_2 site therefore dominate the emission spectrum. An energy level diagram and a typical emission spectrum of nanocrystalline $Y_2O_3:Eu^{3+}$ are shown in Figs. 2.2 (reprinted from Ref. [44]) and 2.3 (reprinted from Ref. [45]), respectively.

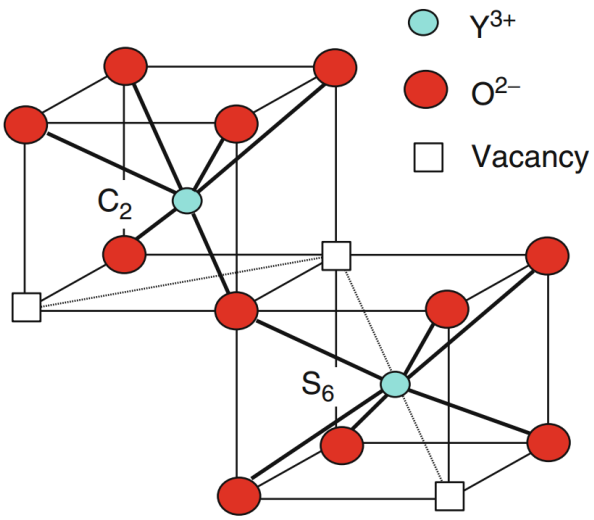

Figure 2.1: *Schematic diagram showing the unique cation sites in the Y_2O_3 lattice.*

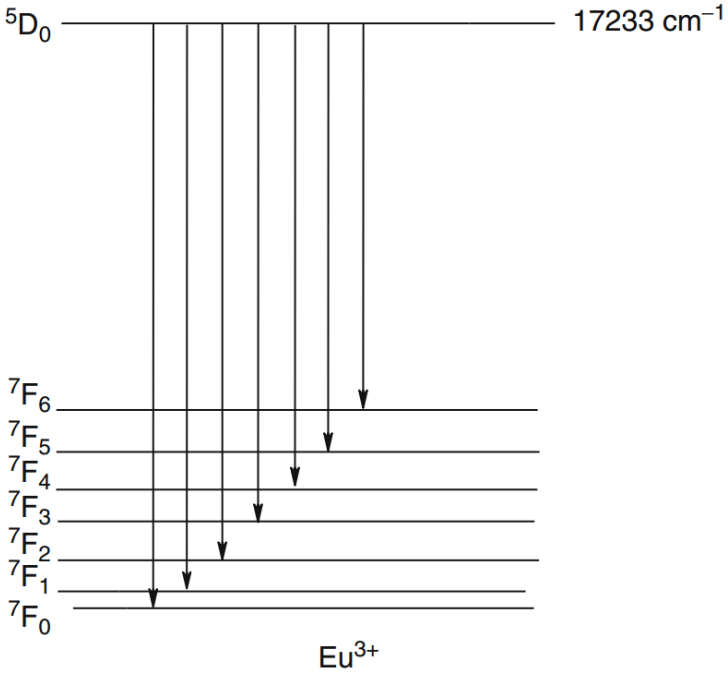

Figure 2.2: *Energy level diagram showing all possible $^5D_0 \rightarrow {}^7F_J$ transitions of the Eu^{3+} ion.*

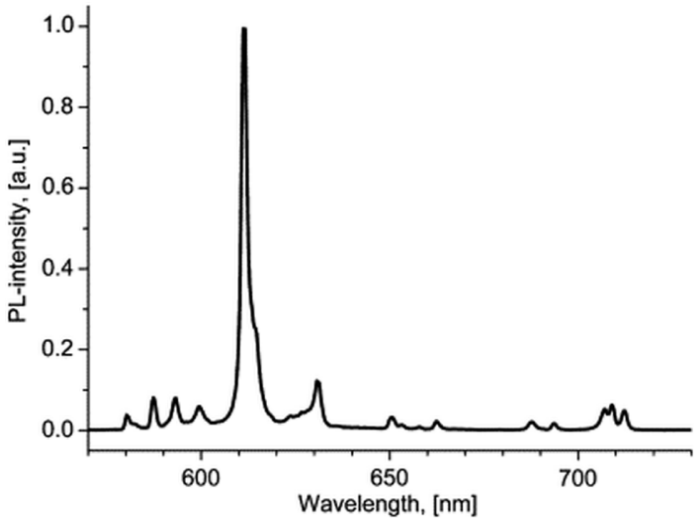

Figure 2.3: *Typical emission spectrum of nanocrystalline $Y_2O_3:Eu^{3+}$.*

2.3 Previous work on spray pyrolysis and $Y_2O_3:Eu^{3+}$

2.3.1 Theoretical and experimental work on spray pyrolysis

The influence of the process parameters on the morphology of powders prepared by spray pyrolysis has been investigated by several research groups over the past decades. Several theoretical models have been developed to predict the particle morphology. Fig. 2.5 shows a schematic overview of which particle morphology can be expected based on the models described below.

Jayanthi *et al.* [46] developed a model for prediction of particle morphology during spray pyrolysis. They compared the characteristic times for the processes occurring during the evaporation step and related these to the morphology of the resulting particle. Zirconium hydroxylchloride, ZrO(OH)Cl, was chosen as model solution. Droplet shrinkage and solute diffusion in the droplet were found to have the large characteristic time constants, i.e. reaching steady state much later than other processes. Vapor diffusion and heat conduction in the gas phase and inside the droplet were found to be much quicker processes. Therefore it was assumed that the quicker processes had reached steady state. It was also assumed that the

solute underwent homogeneous nucleation when and where the solute concentration reached the critical supersaturation concentration (CSC). The crystals formed would then act as seeds for heterogeneous nucleation of the solute where the concentration is equal to or higher than the equilibrium saturation concentration (ESC). Spherical symmetry from the center of the droplet of the center was also assumed. Computational simulations were performed until the solute concentration at the surface of the droplet exceeded CSC. They suggested then that, if the solute concentration at the center of the droplet was higher than the ESC, precipitation would occur throughout the whole volume. If, at the onset of precipitation, the solute concentration at the center of the droplet was lower than ESC a hollow spherical particle would form. Fig. 2.4 shows two different concentrations profiles, where one would lead to volume precipitation and the other surface precipitation. It was observed that a large difference between CSC and ESC was favoring precipitation throughout the whole volume of the droplet. The reason for this is that the concentration needs to be higher than the ESC for precipitation to occur. When there is a large difference between the CSC and the ESC solute will have more time to diffuse towards the center of the droplet before CSC is reached at the surface. Therefore solute concentration at the center will be higher at the onset of precipitation if the difference between CSC and ESC is large. Another important result of their investigation is that a large initial solute saturation also favored volume precipitation. A high initial saturation of the solution would require only a relatively small amount of solute to diffuse to the center of the droplet before the concentration is higher than ESC throughout its volume. For the same reason, low evaporation rate favored volume precipitation. A high evaporation rate would cause a steep solute concentration gradient and decrease the probability for the concentration at the center of the droplet at the onset of precipitation to be higher than ESC. The evaporation rate increases when the relative humidity decreases or the ambient temperature increases.

However, volume precipitation only means solids precipitate throughout the whole volume of the droplet, not that the solids will agglomerate to form a void-free solid particle. Another criterion for the formation of solid void-free particles was therefore proposed. This criterion is the *percolation criterion* which requires the concentration at the center of the droplet at the onset of precipitation is high enough for the solid to fill the volume after precipitation. Percolation theory was used to define a percolation threshold, defined as the lowest concentration of solid particles where a coherent three-dimensional network, i.e. a solid particle, is formed. The volume fraction of solids necessary to create a solid particle is

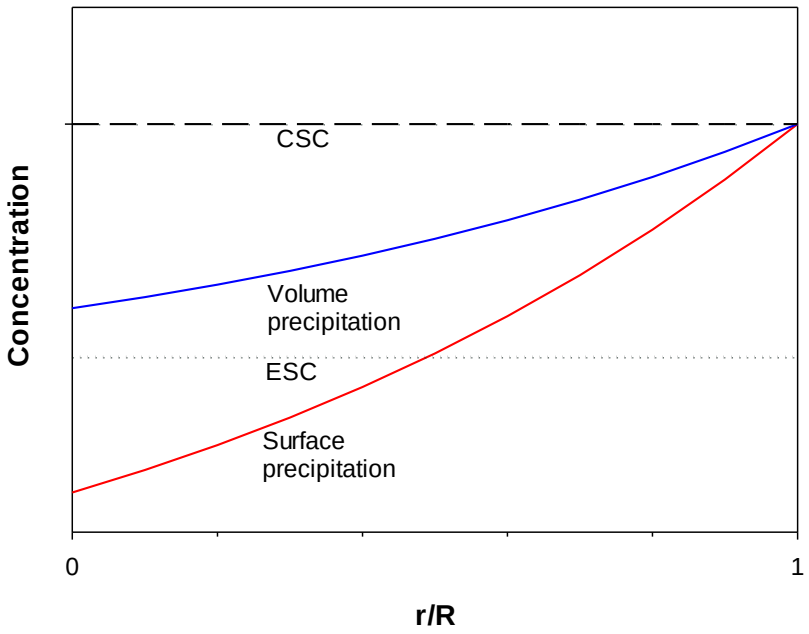

Figure 2.4: *Comparison of two concentration profiles, that at the onset of precipitation would lead to volume precipitation (blue line) and the other to surface precipitation (red line) according to Jayanthi et al.'s model. r and R denotes the distance from the center and the radius of the droplet, respectively. ESC (dotted line) and CSC (dashed line) denotes equilibrium and critical saturation concentration, respectively.*

called the critical volume fraction, φ^*, and is experimentally found to be ~0.16. If the volume fraction, φ, at the center is lower than φ^*, voids would appear. The relationship between φ and the solution concentration, C, is

$$\varphi = \frac{(C)(MW)}{1000\rho} \qquad (3)$$

where MW is the molecular weight and ρ is the crystallographic density of the precipitated solids. If $\varphi < \varphi^*$ a solid particle would not form even if volume precipitation occurs. Thus a critical solution concentration, C^*, can be defined as

$$C^* = \frac{1000\rho\varphi^*}{MW} \quad (4)$$

The percolation criterion therefore requires that ESC ≥ *C** for solid particles to be formed. Otherwise, porous or hollow particles will form. Hence, if solid particles are desired, the solubility of the solute should be higher than *C**.

Another modeling study was performed by Joffin *et al.* [47]. They used Y_2O_3 as model solution and followed much the same approach as Jayanthi *et al [46]*, but also compared their model with experiment. Yttrium nitrate, $Y(NO_3)_3$, dissolved in water was used as precursor solution and atomized by an ultrasonic nozzle. The hot-zone consisted of one drying zone, where the temperature was 225 °C followed by a decomposition/densification zone, where the temperature was 1000 °C. Carrier gas (air) and solution flow rates in the ranges 2.7 – 8.7 m^3 h^{-1} and 5.3 – 16.67 ml min^{-1}, respectively, were considered. In contrast with Jayanthi *et al.* [46] no concentration gradient was observed at the onset of precipitation in this study. According to Jayanthi et al. [46] this would lead to formation of solid or porous particles, if the percolation criterion was met. However, after the thermolysis step the particle were mostly hollow, burst crusts or crust fragments. This apparent error in the model of Jayanthi *et al. [46]* was explained by the fact that the precipitated phase is $Y(NO_3)_3 \cdot 5H2O$ and that water vapor and nitrous gases were released in the decomposition/densification zone and inflated the particles.

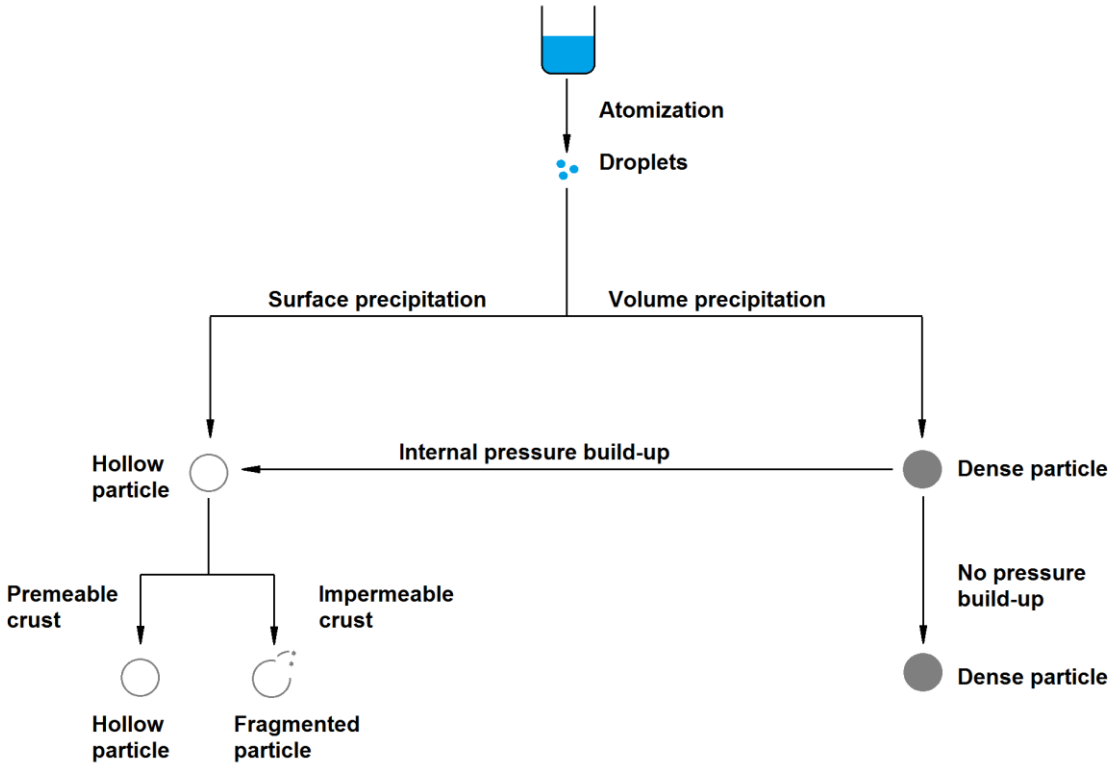

Figure 2.5: *Schematic overview showing which particle morphology can be expected when preparing powders by spray pyrolysis based on the models proposed by Jayanthi et al. and Joffin et al.*

2.3.2 Experimental work on $Y_2O_3:Eu^{3+}$ prepared by spray pyrolysis

Little experimental work has been done on undoped Y_2O_3 prepared by spray pyrolysis. Lanthanide-doped Y_2O_3 has, however, been investigated thoroughly for several decades. Some recent and highly relevant studies of europium-doped Y_2O_3 are presented below.

Moen[39] did an experimental study where he prepared $Y_2O_3:Eu^{3+}$. He investigated the effect of using different complexing agents and precursor solution concentrations. Some of his relevant results of his work are given in Table 2.4. His precursors were $Y(NO_3)_3$ and $Eu(NO_3)_3$. The Eu/Y ratio in the solutions was 0.012. He used the same apparatus as in this work. It had inside diameter and length 20 cm and 100 cm, respectively. The carrier gas was air with a flow of 30 $m^3\ h^{-1}$ and the precursor solution feeding rate was 75 mL min^{-1}. The set

temperature of the furnace was 1000 °C. He prepared eight different samples, where three were non-complexed and two were complexed with maleic acid and three with EDTA. The non-complexed solutions had concentrations 0.05, 0.3 and 0.5 M. The solution complexed with maleic acid had concentrations 0.05 M and 0.5 M, and the solution complexed with EDTA had concentration 0.05, 0.15 and 0.3 M. His samples were calcined at 600 °C for 2 hours. He investigated morphology, crystallite size, specific surface area and luminescence response to UV light and did a thermogravimetric analysis. He found no effect from the precursor solution concentration on any of the characteristics reported in his work. Complexing agents, however, did have a significant effect. Both as-prepared and calcined samples were a mixture of particles with spherical and irregular shapes. The samples prepared from complexed precursor solutions had thinner crusts than those prepared from non-complexed solution. The size of the spherical particles was a few micrometers, but it was not quantified. Moen[39] also claimed that the samples prepared from precursor solutions complexed with maleic aid were dense or nanoporous. X-ray diffraction was used to determine phase purity and crystallite sizes by the Scherrer equation[48] and Rietveld refinement[49]. The two samples prepared from solutions complexed with maleic acid contained small amounts of yttrium oxycarbonate, $Y_2O_2CO_3$. The thermogravimetric analysis was performed on three as-prepared samples. The samples were heated up to 1000 °C with 10 °C min^{-1} heating rate. The analyzed samples were one from non-complexed precursor solution, one from precursor solution complexed with maleic acid and one from precursor solution complexed with EDTA. The respective precursor solution concentrations the analyzed samples were prepared from were 0.5, 0.5 and 0.3 M. The sample prepared from non-complexed solution had a weight loss of 13 %, while the weight losses of the samples prepared from solutions complexed with maleic acid and EDTA were 39 and 50 %, respectively. During calcination the weight losses of these samples were 16, 47 and 43 %, respectively. Luminescence response was investigated by using a UV lamp and visual inspection by the naked eye, i.e. no quantitative measurements. When exposed to light with 254 nm wavelength, all samples had a red-orange glow. When changing the wavelength to 366 nm, no visible light was observed, except from the samples prepared from precursor solution complexed with maleic acid. These samples then had a pale purple glow. Moen[39] claimed this was due to an alteration of the emission spectrum of these samples.

Table 2.4: *Results obtained by Moen's preparation of Y_2O_3:Eu^{3+} by spray pyrolysis. d, SA and D are the crystallite size, specific surface area and particle size calculated from the specific surface area, respectively.*

	As-prepared	**Calcined**			
Sample (Complexing agent / precursor solution concentration [M])	*d* [nm]	*SA* [m^2 g^{-1}]	*D* [nm]	*d* [nm] (Scherrer)	*d* [nm] (Rietveld)
None / 0.05	9.6	21	57	13.6	15.3
None / 0.03	7.9	26	46	14.0	14.2
None / 0.5	8.8	31	38	14.7	15.7
Maleic acid / 0.05	8.6	21	57	12.6	13.5
Maleic acid / 0.5	7.4	21	57	12.7	13.3
EDTA / 0.05	3.3	39	31	11.5	13.4
EDTA / 0.15	3.8	39	31	11.3	13.5
EDTA / 0.3	6.9	42	28	11.0	12.5

Sohn *et al.*[50] prepared europium-doped Y_2O_3, Y_2O_3:Eu^{3+} by spray pyrolysis. Their process involved a pilot-scale unit using an ultrasonic droplet generator. The length and inside diameter of the hot-zone was 120 cm and 5 cm, respectively, and the temperature was fixed at 900 °C. The carrier gas (air) flow rate was 2.7 m^3 h^{-1} and the residence time of the droplets was 0.65 s. Yttrium and europium nitrates dissolved in water were used as precursor solution. The Eu^{3+}/Y^{3+} ratio in the precursor solution was held at 6 at%, while the total concentration of the cations was fixed at 0.7 M. Citric acid and ethylene glycol were added to the precursor solution with concentrations varying from 0 M to 0.47 M and 0 M to 0.35 M, respectively. As-prepared particles were calcined at 1150 °C for 3 h. Average crystallite sizes were calculated by the Scherrer equation.

Morphologies and crystallite sizes of the particles before calcination (i.e. as-prepared particles) were not specified. Without addition of citric acid and ethylene glycol, the particles had spherical and hollow morphology and were non-agglomerated. Average crystallite size was 33 nm. When only citric acid was added to the precursor solution, the particles were porous and had a non-spherical shape and a thin-walled structure. It was proposed that evolution of gaseous products from the decomposition of citric acid caused pressure build-up inside the particles and bursting of the particles. Average crystallite size was 32 nm. With addition of both citric acid and ethylene glycol to the precursor solution a viscous gel was formed inside the particles, and their morphology was dense and spherical. Average crystallite size was in this case 49 nm. Of all samples, the one prepared from solution containing citric

acid and no ethylene glycol had the lowest photoluminescence intensity of all samples. The luminous intensity of this sample was only 35–40 % of that of the sample prepared from non-complexed precursor solution, which displayed the second highest intensity.

Marinkovic *et al*.[51] investigated the effect of europium doping level and crystallite and particle size on the photoluminescent properties of Y_2O_3:Eu^{3+}. Powders were prepared from a precursor solution containing yttrium and europium nitrates with cation concentration 0.1 M. An ultrasonic droplet generator with vibration frequency 1.3 MHz was used to atomize the precursor solution. The hot-zone of their apparatus was divided into three subzones, with temperatures 200 °C, 700 °C and 900 °C. The carrier gas (air) flow rate was 0.06 m^3/h. Residence time in the hot-zone was 68 s. The size of the reactor tube was not specified. As-prepared powders were calcined at 1000 °C, 1100 °C and 1200 °C for 12 h. Crystallite sizes were estimated by Rietveld refinement. Average particle sizes were estimated using a semi-automated image analysis software on their SEM micrographs. Photoluminescence spectra and lifetime measurements were obtained by spectrofluorometry.

As-prepared samples had average crystallite size 19 nm, while after calcination at 1000 °C it increased to 41 nm. It was found that for these processing conditions the particles were spherical, dense and un-agglomerated. They were all in the 300–800 nm range. The particle morphology remained unchanged when calcined for all temperatures, except when calcined at 1200 °C, where intraparticle sintering occurred. Doping level did affect neither crystallite size nor particle size notably. Best photoluminescent performance was achieved for the samples with 5 % europium-doping. The samples with the highest and lowest photoluminescence intensity were, respectively, the sample calcined at 1000 °C and the as-prepared one. The intensity of the as-prepared sample relative to the one calcined at 1000 °C was about 35 %.

Roh *et al.[52]* investigated the effect adding citric acid (CA) and polyethylene glycol (PEG) with and average molecular weight of 200 g mol^{-1} to the precursor solution. Yttrium and europium nitrates were used as cation sources. The cation concentration of the precursor solution was 0.8 M and the doping concentration was 6 at%. Concentrations of CA and PEG in the precursor solution were varied between 0 and 0.6 M, and 0 and 0.3 M, respectively. The precursor solution was atomized by an ultrasonic atomizer (1.7 MHz). Length and inside diameter of their tubular flow reactor were 120 and 5 cm, respectively and the carrier gas (air) flow rate was 2.7 m^3 h^{-1}, giving a residence time of 0.6 s. The temperature of the reactor was

fixed at 900 °C. All as-prepared samples were calcined at 1150 °C for 3 h. The Scherrer equation was used for estimation of the crystallite sizes.

Without addition of any organic components in the precursor solution the particles were porous and had a fragmented empty sphere-like structure after calcination. After calcination the average crystallite size was 42 nm. When the concentration of CA was 0.3 M and no PEG was added to the precursor solution the particles were highly irregular and no spherical particles could be observed. Unfortunately, average crystallite size was not stated for this sample. When the concentrations of CA and PEG were higher than 0.1 and 0.3 M, respectively, the particles were dense and spherical with smooth surfaces. The crystallite sizes were not stated for all samples, but it was noted that the crystallite size was smaller when the morphology of the particles were irregular. Best luminescence performance was obtained for samples prepared from solutions containing both CA and PEG. The sample prepared from precursor solution complexed with CA without PEG had the poorest luminescence performance. Its intensity was about 60 % lower than for the sample prepared from non-complexed precursor solution. In turn, the sample prepared from non-complexed precursor solution had 45 % lower intensity than the samples prepared from solutions containing both CA and PEG. The high intensity was ascribed to smooth surfaces with low concentrations of defects and large crystallite size.

Koo *et al.[53]* studied the effect of addition of ethylenediaminetetraacetic acid (EDTA), CA and boric acid (BA) to the precursor solution when preparing Y_2O_3:Eu^{3+}. Yttrium and europium nitrates were used as cation sources. The total concentration of the cations was 0.1 M, but the relative concentration of Y and Eu was not specified. Thus, the exact composition is not known. Four different precursor solutions were investigated: no organic additives, 0.1 M EDTA, 0.2 M EDTA and 0.1 M EDTA + 0.1 CA. BA was used as flux and the amount was fixed at 1 wt% of Y_2O_3:Eu^{3+} powders. They used an ultrasonic droplet generator (1.7 MHz) and air as carrier gas with a flow rate of 3 m^3 h^{-1}. The hot-zone temperature was fixed at 900 °C. Calculated residence time was 0.5 s. The powders were calcined between 950 and 1250 °C for 3 h. Crystallite sizes were determined by using the Scherrer equation on x-ray diffractograms. The value of the shape factor was not stated. Photoluminescence performance was studied using a D_2 lamp. No further explanation of how these measurements were performed was given.

The as-prepared powders were all hollow and spherical and had submicronic sizes. Addition of organic compounds increased the hollowness and gave the powders thinner crusts. Calcination at 1150 °C caused the particles to lose their sphericity and a loosely aggregated sponge-like morphology was observed. Unfortunately, crystallite sizes were reported only for some of the samples. The sample prepared from the precursor solution without organic additives had average crystallite size 20, 40, 44 and 62 nm when calcined at 950, 1050, 1150 and 1250 °C, respectively. When calcined at 1150 °C the average crystallite sizes for the samples prepared from precursor solutions without organic additives, 0.1 M EDTA, 0.2 M EDTA and 0.1 M EDTA + 0.1 M CA were 44, 37, 42 and 44 nm, respectively. The photoluminescence intensity of the samples calcined at 1150 °C was highest for the sample prepared with 0.1 M EDTA and 0.1 M CA, followed by the samples containing 0.2 M EDTA, no additives and 0.1 M EDTA. The low intensity of the 0.1 M EDTA sample was assigned to small crystallite size and the irregular shape of the particles.

When looking at all the studies referred to above, some trends seem to appear. Addition of compexing agents (EDTA, maleic acid, citric acid) to the precursor solution has a considerable effect on particle morphology. Particles prepared from complexed precursor solutions were more porous with thinner crusts and a greater fraction had irregular morphology. Without addition of any organic additives to the precursor solution the particles were more spherical and less porous. Only by addition of alcohols and complexing agents were dense particles with smooth surfaces been obtained. Moen's[39] work is the only study standing out from this trend. He claimed that the precursor solution complexed with maleic acid yielded particles with smooth surfaces. Slightly different experimental setups (organic additives, residence times, set temperatures of the furnaces and calcination programs) make the crystallite sizes difficult to compare. As would be expected, higher calcination temperature and longer calcination time gave larger crystallites, and the studies agree well with each other. The photoluminescence performance appeared to be affected by the particle morphology. Samples with large fractions of particles with irregular morphology consistently had lower luminous intensity than the samples with more spherical particle morphologies. As a consequence, samples prepared from complexed precursor solutions had generally lower intensities.

To the author's knowledge, Moen's[39] study is the only where the effect of adding maleic acid to the precursor solution has been investigated.

3 Experimental

3.1 Powder preparation

A flowchart for the preparation of precursor and powder is shown in Fig. 3.1. $Y(NO_3)_3 \cdot 6H_2O$ (99.8 %, Sigma Aldrich) and $Eu(NO_3)_3 \cdot 6H_2O$ (99.9 %, Alfa Aesar) were dissolved in distilled water to a concentration of ~1 M and 0.1 M, respectively, and left stirring overnight. The solutions were then thermogravimetrically standardized at 1200 °C. The standardized solutions were split into three equal parts. One part was complexed with maleic acid, one with ethylenediaminetetraacetic acid and one was left uncomplexed. Their chemical structures are shown in Fig. 3.3. For both the two complexed solutions, the complexing agent : (Y^{3+}, Eu^{3+}) ratio was 2:1. The complexed solutions were again left stirring overnight. The three solutions were then diluted by addition of distilled water into a concentration of 0.05 M of the cation. Each solution was then split into ten equal parts, so that the total number of precursor solution batches was 30. Europium solution was added to three of the precursor solution batches. The amount of europium was 1.5 at% of the cations, so that the composition of the product was $(Y_{0.985}Eu_{0.015})_2O_3$. The volume of each precursor solution batch was fixed so that without any loss of powder, full conversion and no contamination would yield 10 g of $(Y_{1-x}Eu_x)_2O_3$ powder.

Powders were prepared by spray pyrolysis. Fig. 3.2 shows a schematic overview of the apparatus used for the preparation. The solutions were atomized by a two-fluid atomizer, where the solutions and pressurized air (150 kPa) were mixed internally in a nozzle and sprayed into the hot-zone. Air was used as carrier gas. Table 3.1 shows which complexing agent, carrier gas flow, F_{cg}, solution feeding rate, F_s, and amount of europium was used for the different samples. Between all samples distilled water was sprayed into the hot-zone for 5 minutes at ~150 mL min^{-1} before turning the feeding rate down to ~10 mL min^{-1}, turning off the carrier gas flow and replacing the powder collector with a clean one. The distilled water feeding rate was then turned up to ~150 mL min^{-1} and carrier gas flow turned on again. The set hot-zone temperature was 1000 °C.

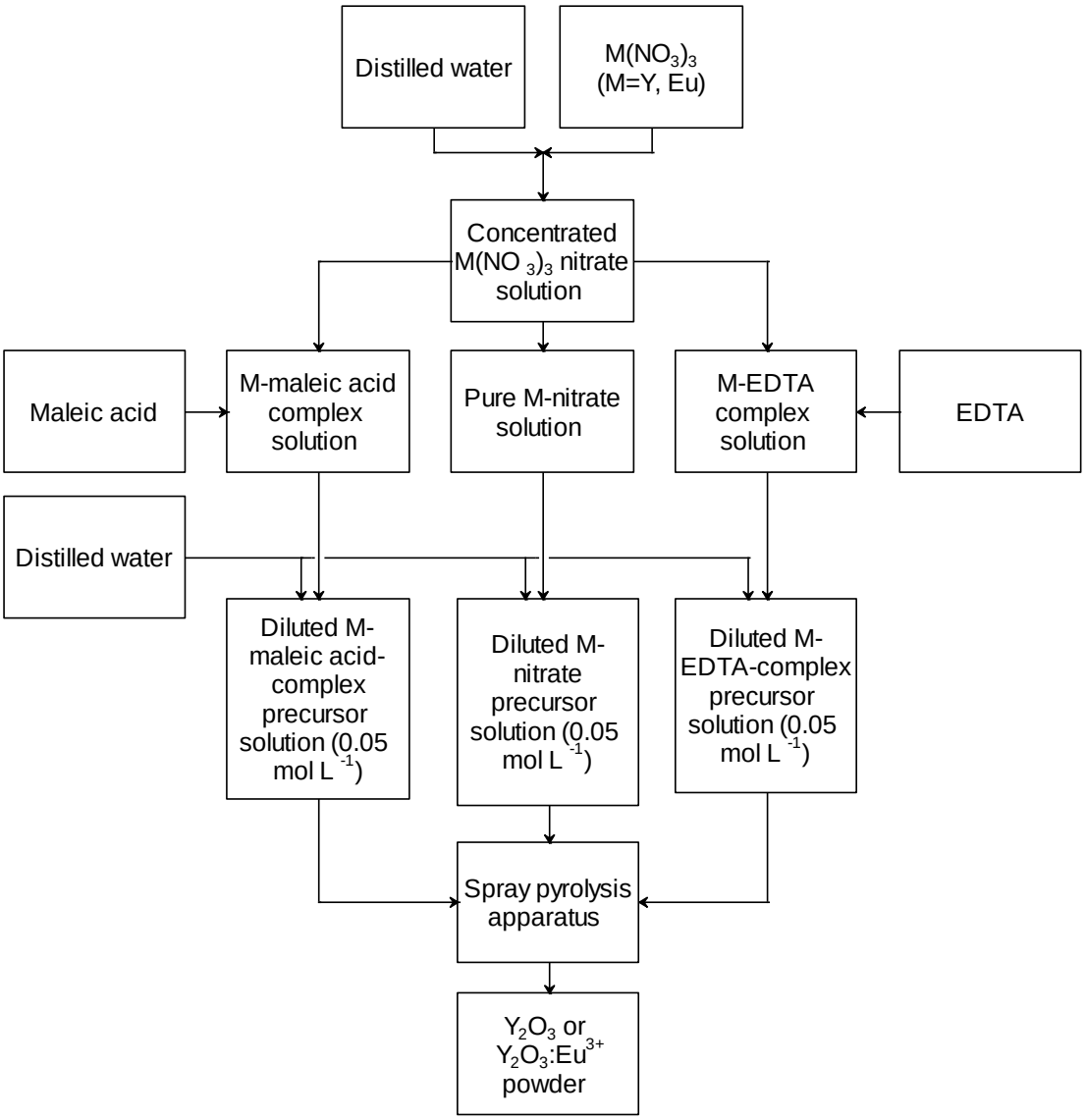

Figure 3.1: *Flowchart showing the steps of the preparation of Y_2O_3 and $Y_2O_3:Eu^{3+}$.*

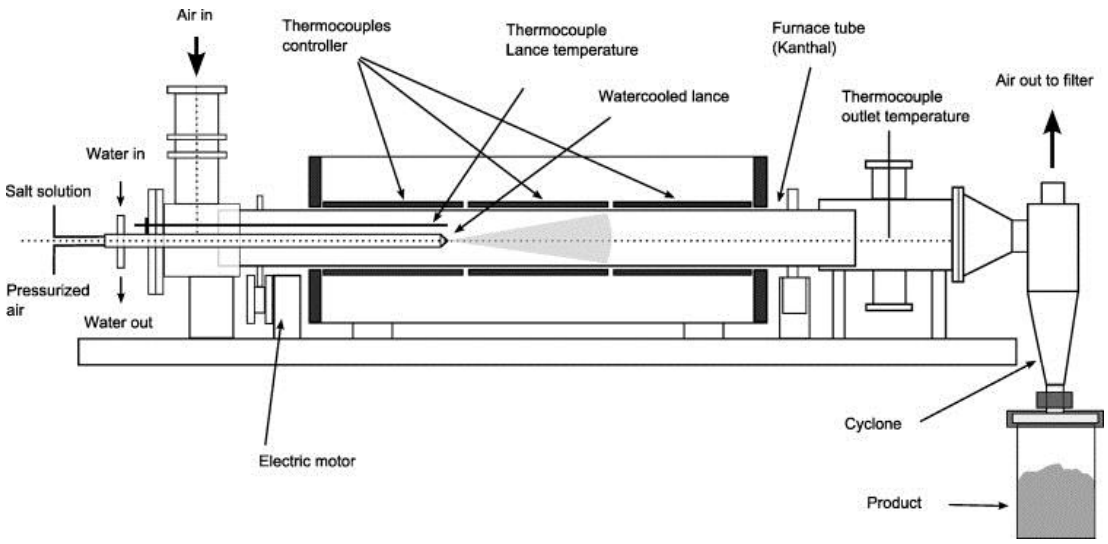

Figure 3.2: *Schematic overview of the spray pyrolysis apparatus used in this work.*

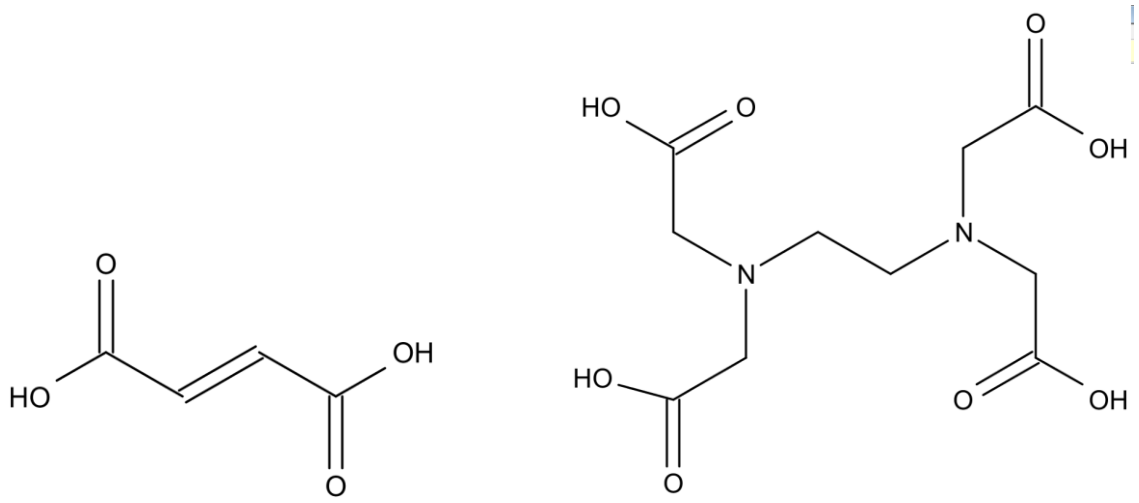

Figure 3.3: *Chemical structures of maleic acid (left) and EDTA (right).*

Table 3.1: *Overview of the different samples prepared and their respective abbreviation, complexing agent, flow rates of carrier gas and precursor solution and europium content.*

Sample abbreviation	**Complexing agent**	**Precursor solution feeding rate, F_s [mL min^{-1}]**	**Carrier gas flow, F_{cg} [m^3 h^{-1}]**	**Europium content (x in $(Y_{1-x}Eu_x)_2O_3$)**
N-75-15	None	75	15	0
N-150-15	None	150	15	0
N-300-15	None	300	15	0
N-75-30	None	75	30	0
N-150-30	None	150	30	0
N-300-30	None	300	30	0
N-75-40	None	75	40	0
N-150-40	None	150	40	0
N-300-40	None	300	40	0
N-75-30-Eu	None	75	30	0.015
M-75-15	Maleic acid	75	15	0
M-150-15	Maleic acid	150	15	0
M-300-15	Maleic acid	300	15	0
M-75-30	Maleic acid	75	30	0
M-150-30	Maleic acid	150	30	0
M-300-30	Maleic acid	300	30	0
M-75-40	Maleic acid	75	40	0
M-150-40	Maleic acid	150	40	0
M-300-40	Maleic acid	300	40	0
M-75-30-Eu	Maleic acid	75	30	0.015
E-75-15	EDTA	75	15	0
E-150-15	EDTA	150	15	0
E-300-15	EDTA	300	15	0
E-75-30	EDTA	75	30	0
E-150-30	EDTA	150	30	0
E-300-30	EDTA	300	30	0
E-75-40	EDTA	75	40	0
E-150-40	EDTA	150	40	0

(Table 3.1 continued)

E-300-40	EDTA	300	40	0
E-75-30-Eu	EDTA	75	30	0.015

All as-prepared samples were calcined in air at 600 °C. Samples for infrared spectroscopy were also heat treated at 200 and 400 °C. Heating and cooling rates were ~200 °C h^{-1} and holding time was 2 h in all cases. Hereafter, samples heat treated at 600 °C will be referred to as «calcined» or «calcined at 600 °C », and samples treated lower temperatures as «heat treated».

3.2 Powder characterization

3.2.1 X-ray diffraction (XRD)

X-ray diffractograms were obtained from as-prepared and calcined samples in a Bruker AXS D8 Focus diffractometer with a Cu Kα radiation source (wavelength λ = 1.5418 Å) and a 0.2 mm slit. Data were collected in the 2θ range 10–60°, using a 0.1° step size and step time 10 s. Crystallite sizes were estimated from the (222) Bragg reflection at 29.1° using the Scherrer equation:

$$d = \frac{0.9\lambda}{\beta\cos\theta} \quad (5)$$

where β is the full width at half maximum.

3.2.2 Scanning electron microscopy

Particle size and morphology were investigated in a Zeiss Supra 55 VP low vacuum field emission scanning electron microscope with a secondary electron detector. Working distance and accelerating voltage were 10 mm and 12 kV, respectively.

3.2.3 Gas adsorption

Specific surface area was measured by gas adsorption in a Micromeritics TriStar 3000 using nitrogen as adsorption gas. All samples were degassed in vacuum at 250 °C overnight. For estimation of particle size, particles were assumed to be monodisperse and spherical, and calculated from the equation

$$D = \frac{6}{\rho(SA)} \qquad (6)$$

where ρ is the crystallographic density and SA is the measured specific surface area.

3.2.4 Infrared spectroscopy

Infrared spectroscopy measurements were performed in a Bruker IFS 66v Fourier Transform Infrared spectrometer on potassium bromide (spectroscopic grade, Merck) pellets containing 0.2 wt% of the powder sample. Only as-prepared, heat treated and calcined samples prepared with precursor solution feeding rate 75 mL min^{-1} and carrier gas flow rate 30 m^3 h^{-1} were investigated.

3.2.5 Photoluminescence

Photoluminescence emission spectra were recorded from calcined N-75-30-Eu, M-75-30-Eu and E-75-30-Eu using a Leica DM5500B photoluminescence microscope with an ASI Hyperspectral scanner. A PRIOR Lumen 200 illumination system was used as excitation source. Spectra were recorded in the 400 – 800 nm range with 4 nm resolution by the LabView software. Before examination, the samples were pressed into pellets by a uniaxial press. The spectra were recorded from the brightest point in the samples.

4 Results

4.1 Appearance

The uncomplexed precursor solutions yielded a greyish white or off-white powder with the highest tapped density. Precursor solutions with complexing agents yielded a dark brown or grey fluffy powder with low tapped density. All samples turned white or light greyish white and increased their tapped density after calcination at 600 °C. The samples prepared with precursor solution feeding rate 75 mL min^{-1} and carrier gas flow rate 15 m^3 h^{-1}, which were also heat treated at 200 and 400 °C, turned white only after calcination at 600 °C. A photograph showing the how the color of the samples prepared with precursor solution feeding rate 75 mL min^{-1} and carrier gas flow rate 30 m^3 h^{-1} changed with thermal treatment is shown in Fig. 4.1.

N-150-15, M-150-15 and E-300-15 yielded moist powders or a thick slurry-like mixture of powder and water when collected in the powder collector. After calcination all samples had increased tapped density.

4.2 Production yield

The yield of production of each sample was calculated by the following formula:

$$Yield = \frac{m_b m_c/m_s}{m_0} \times 100\ \% \qquad (7)$$

where m_b is the mass of all powder collected from the sample, m_c/m_s is the ratio between the mass of the sample after and before calcination and m_0 = 10 g is the mass of an ideal sample. Table 4.1 presents the mass of powder collected, relative weight loss during calcination and yield of each of the prepared samples. The yield ranged between 9 and 88 %, but the great majority of the samples had a yield in the range between 40 and 60 %. The yield was not significantly affected by any of the parameters varied in the synthesis.

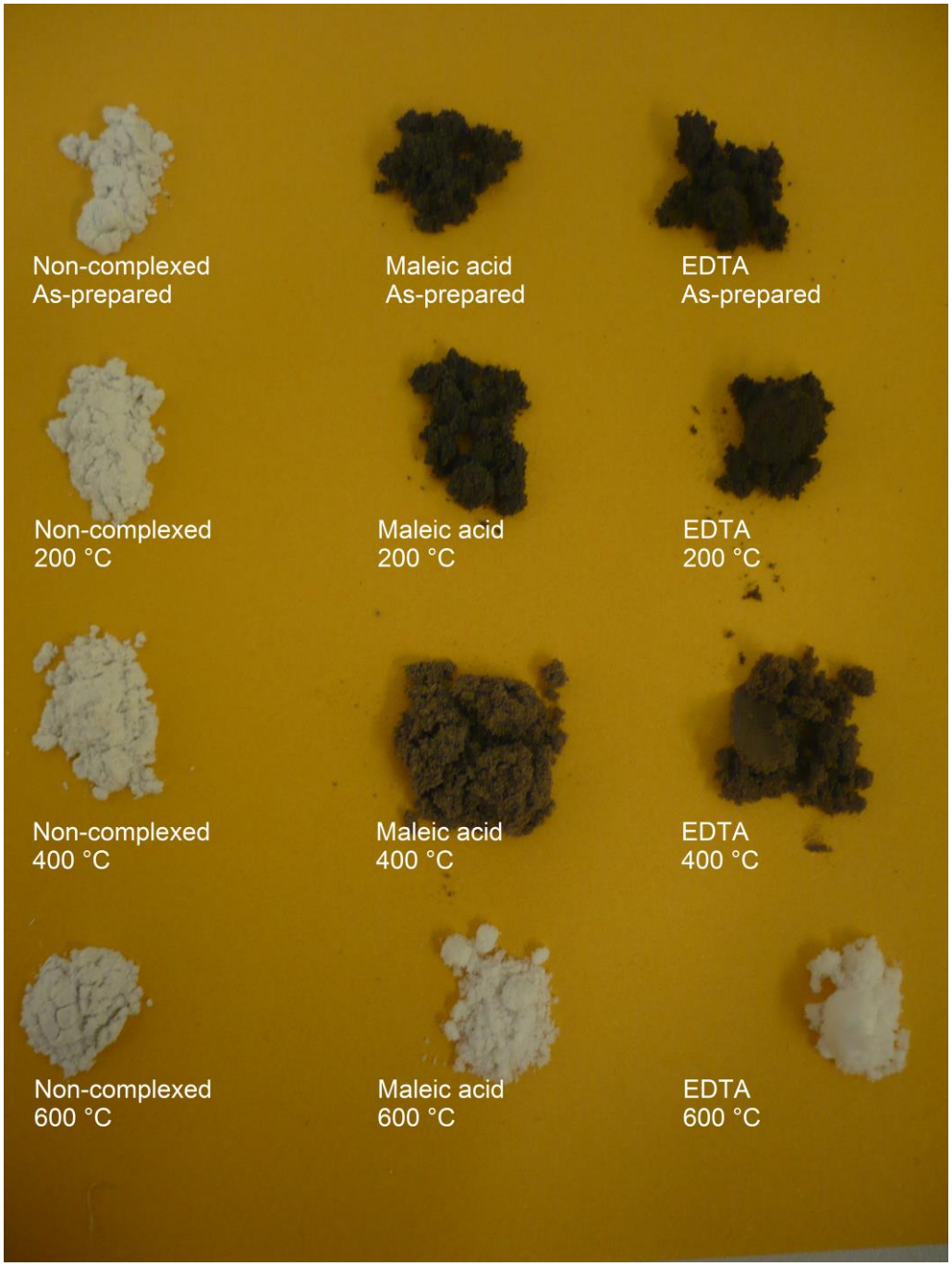

Figure 4.1: *Overview of the color of samples prepared with precursor solution feeding rate 75 mL min^{-1} and carrier gas flow rate 15 m^3 h^{-1} as-prepared and after heat treatment and calcination.*

Table 4.1: *Total mass collected in the powder collector, ratio between the weight of calcined and as-prepared sample and the yield of each prepared sample.*

Sample	m_b	m_c/m_s	**Yield [%]**
N-75-15	0.9	0.95	9
N-150-15	11.2	0.31	35
N-300-15	14.7	0.6	88
N-75-30	3.5	0.93	33
N-150-30	6.0	0.91	55
N-300-30	8.0	0.80	64
N-75-40	4.8	0.88	42
N-150-40	6.8	0.83	56
N-300-40	6.7	0.76	51
N-75-30-Eu	1.4	0.91	13
M-75-15	10.9	0.48	52
M-150-15	17.8	0.25	45
M-300-15	13.8	0.45	62
M-75-30	11.0	0.45	50
M-150-30	12.6	0.51	64
M-300-30	14.7	0.37	54
M-75-40	10.1	0.52	53
M-150-40	11.2	0.47	53
M-300-40	2.8	0.53	15
M-75-30-Eu	14.2	0.39	55
E-75-15	9.3	0.43	40
E-150-15	20.9	0.24	50
E-300-15	15.2	0.3	46
E-75-30	10.0	0.55	55
E-150-30	11.5	0.50	58
E-300-30	12.4	0.40	50
E-75-40	12.3	0.47	58

(Table 4.1 continued)

E-150-40	11.5	0.45	52
E-300-40	11.1	0.39	43
E-75-30-Eu	9.2	0.62	57

4.3 X-ray diffraction

X-ray diffractograms of as-prepared and calcined samples are shown in Fig. 4.2. As-prepared N-150-15 was too moist to be suited for these experiments. The diffractograms of as-prepared samples are mostly in agreement with the standard data for cubic Y_2O_3 (space group *Ia-3*). As-prepared N-75-15, N-75-30-Eu, N-75-40, N-150-40, N-300-40 and E-75-15 also included diffraction peaks from other phases. The secondary phase in N-75-15 was $La_{0.6}Sr_{0.4}Co_{0.2}Fe_{0.8}O_3$ (hereafter referred to as LSCF), the composition produced by the previous user of the apparatus. The additional diffraction peaks in the diffractograms of N-75-30-Eu, N-75-40, N-150-40 and N-300-40 were not consistent with any phases found in the database. The low 2θ values for these peaks might indicate a large distance between atomic planes, often the case with organic compounds. As-prepared M-300-30, M-75-40, M-150-40, M-300-40, E-75-30, E-75-30-Eu and E-75-40 and gave only very weak or no peaks at all in their diffractograms. These samples did therefore not have a long-range ordering of their atoms, and were most likely of too low crystallinity or amorphous. Secondary phases were also detected in calcined N-75-15, N-75-30-Eu, M-75-30, M-150-30 and M-300-30. The additional diffraction peaks in the diffractograms of calcined N-75-15 and N-75-30-Eu are at the same 2θ values as in the diffractograms of their as-prepared counterparts, and are assigned to the same phases. The diffractograms of M-75-30, M-150-30 and M-300-30 included additional diffraction peaks consistent with $Y_2O_3CO_3$. All other diffractograms of calcined samples are in agreement with the standard data for cubic Y_2O_3. For all samples except E-300-40, diffraction peaks were narrower in calcined samples.

Crystallite sizes of as-prepared and calcined samples calculated by Eq. 1 and crystallite sizes and unit cell lengths of calcined samples found by Rietveld refinement are presented in Table 4.2. The parameters varied in this work did not affect the crystallite sizes to a noticeable

extent. Except for E-300-40, the sample with broader peaks after calcination, all samples grew larger upon calcination. Eq. 1 gave as-prepared crystallite sizes in the range 11–19 nm. Crystallite sizes of calcined samples estimated by Eq. 1 and Rietveld refinement were in the ranges 11 – 28 and 14 – 21 nm, respectively. Rietveld refinement generally estimated a larger crystallite size than Eq. 1. There was only one exception from this trend, E-300-30, where Eq. 1 estimated the average crystallite size to be 23 nm, whereas Rietveld refinement estimated 22 nm. The unit cell parameters of the calcined samples varied between 10.603 and 10.621 Å. The smallest value was found for N-75-15 and the largest for M-75-30. However, for both these samples, secondary phases were observed in the diffractograms, which may have affected the value. Among the phase pure samples, the smallest unit cell length was 10.610 Å, found for E-75-15, E-300-15 and E-300-30, while E-300-40 had the largest with 10.619 Å. These values are slightly larger than the values reported in the literature (10.602 – 10.604 Å[21, 54]).

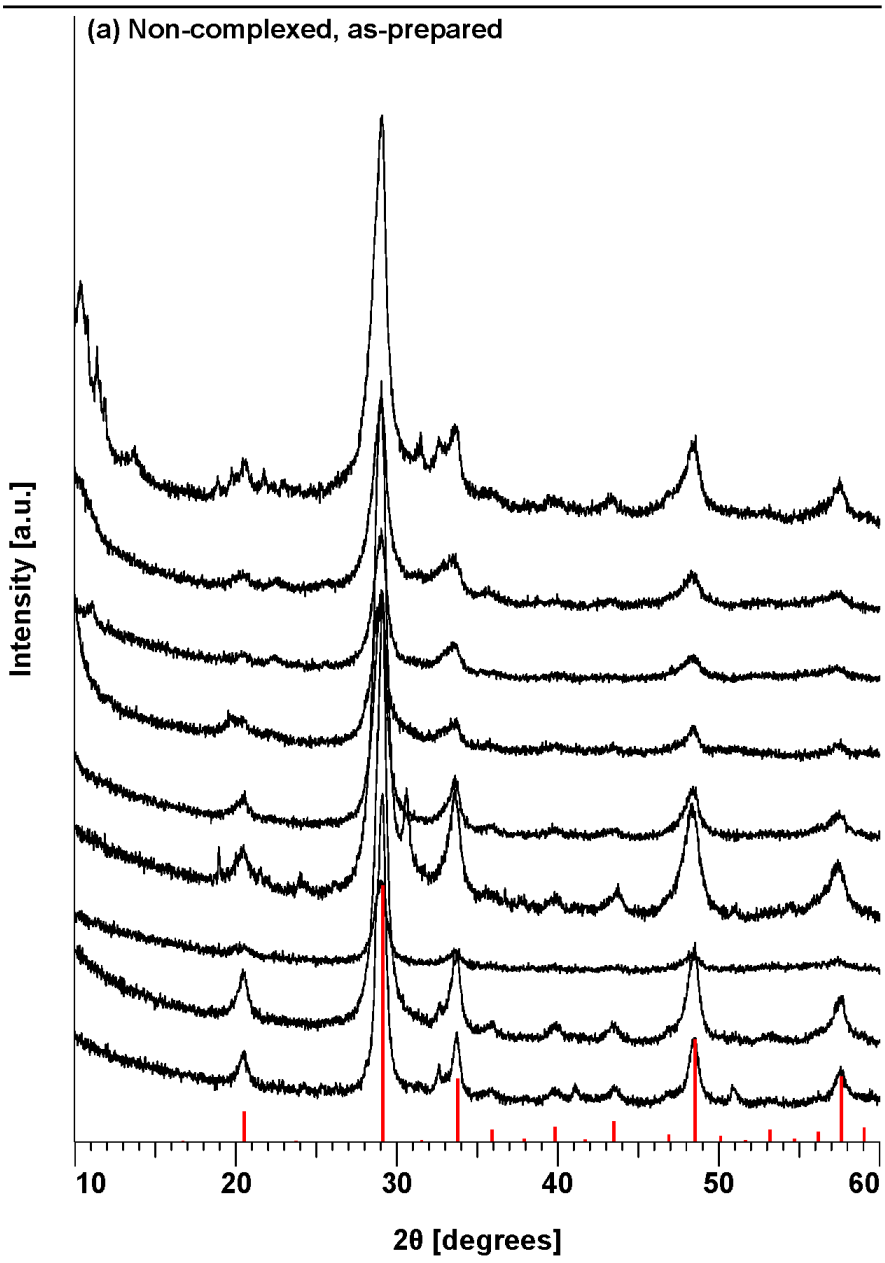

(Fig. 4.2 continues)

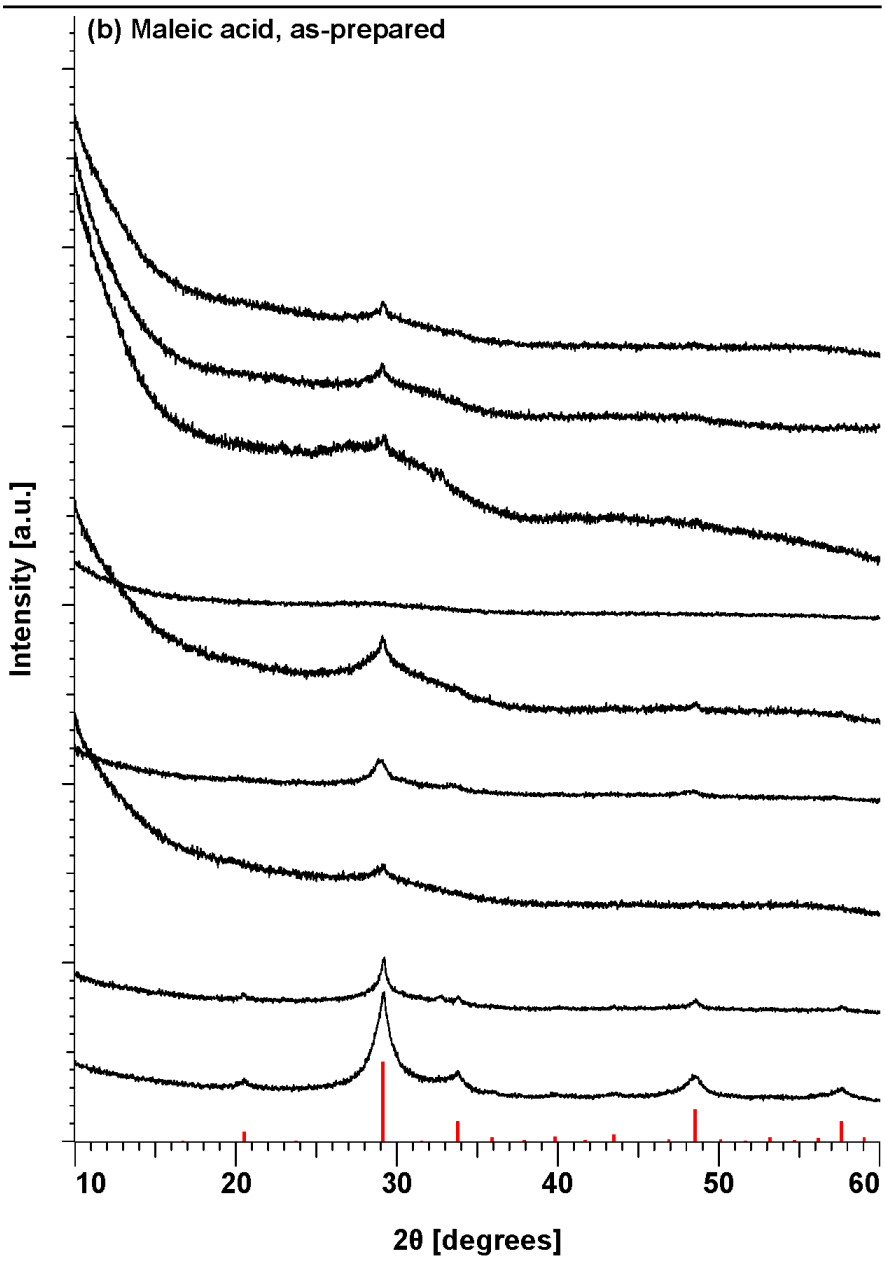

(Fig. 4.2 continues)

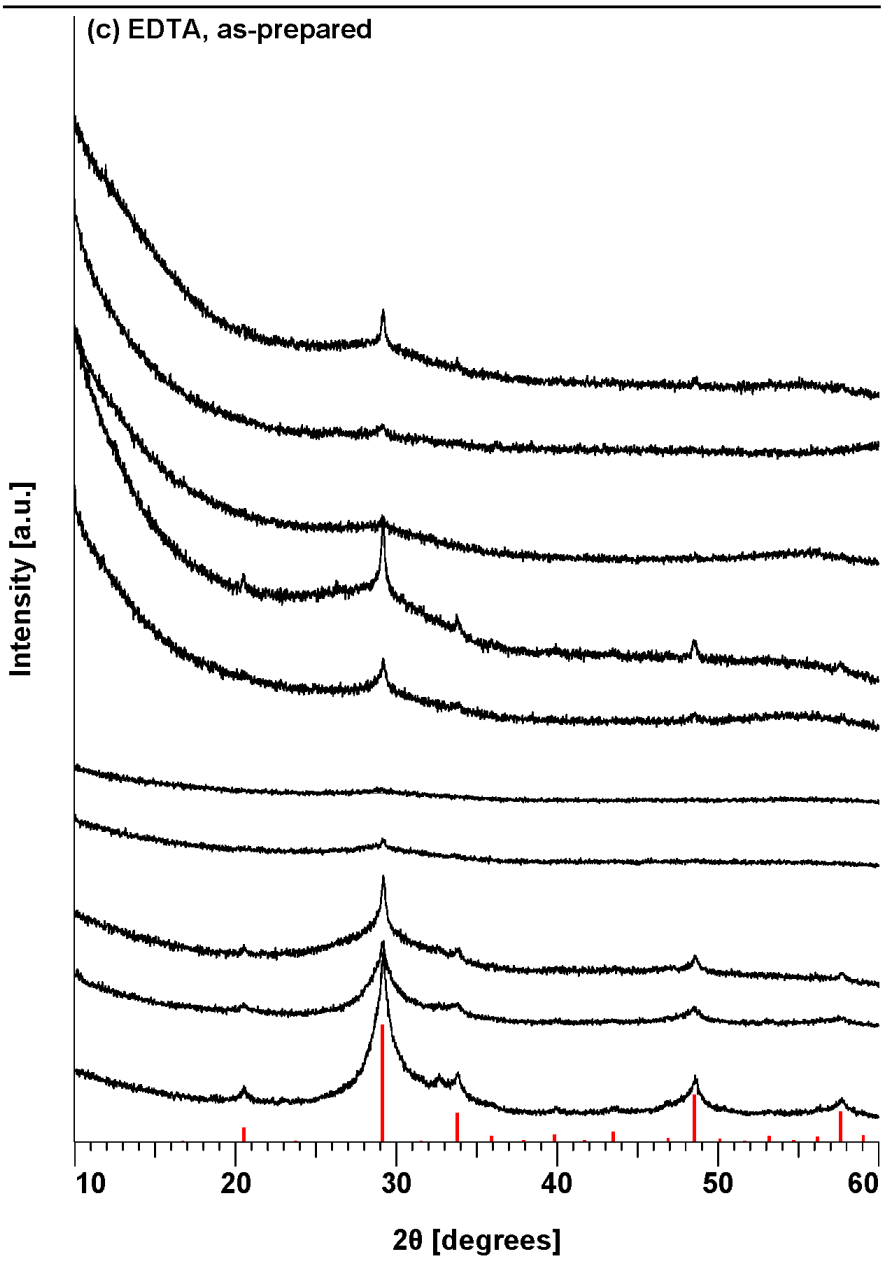

(Fig. 4.2 continues)

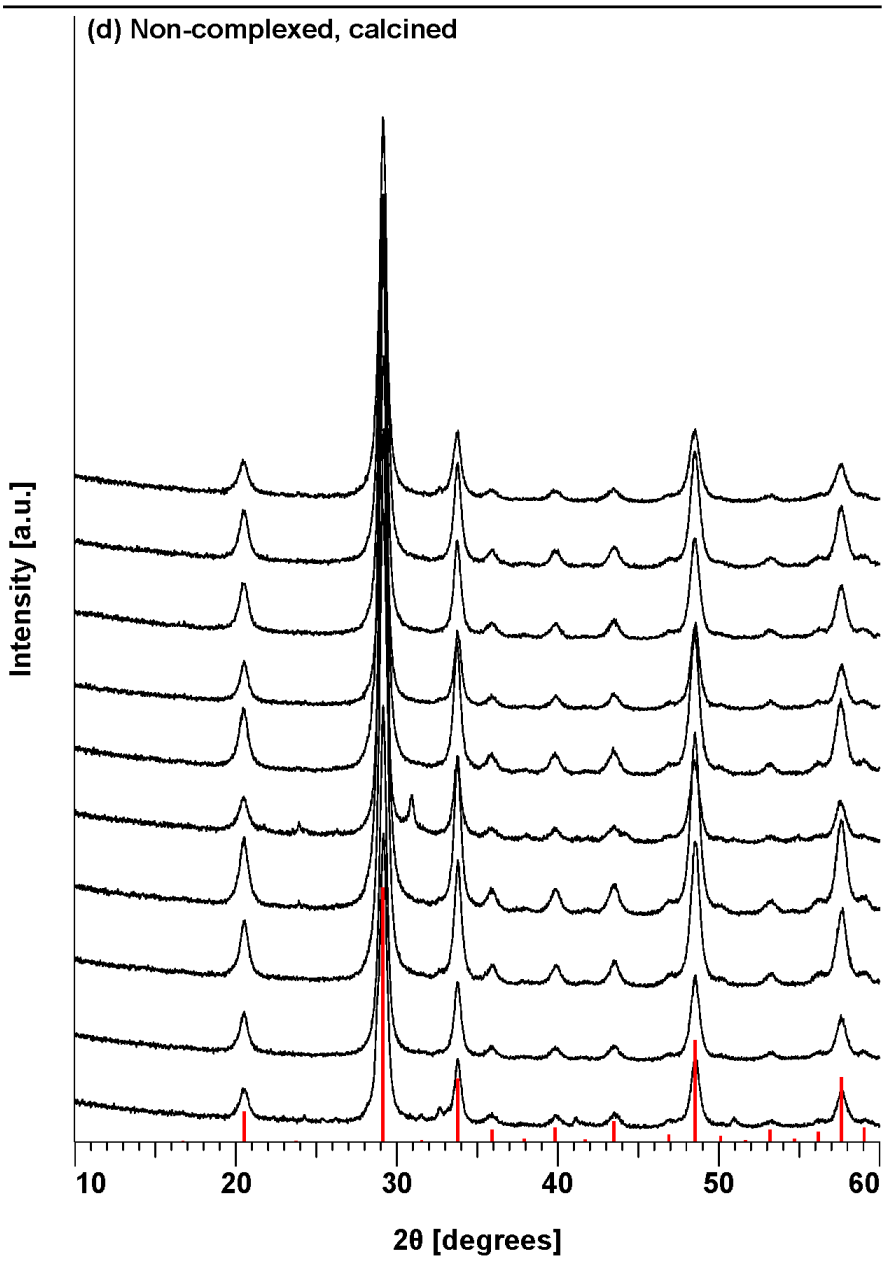

(Fig. 4.2 continues)

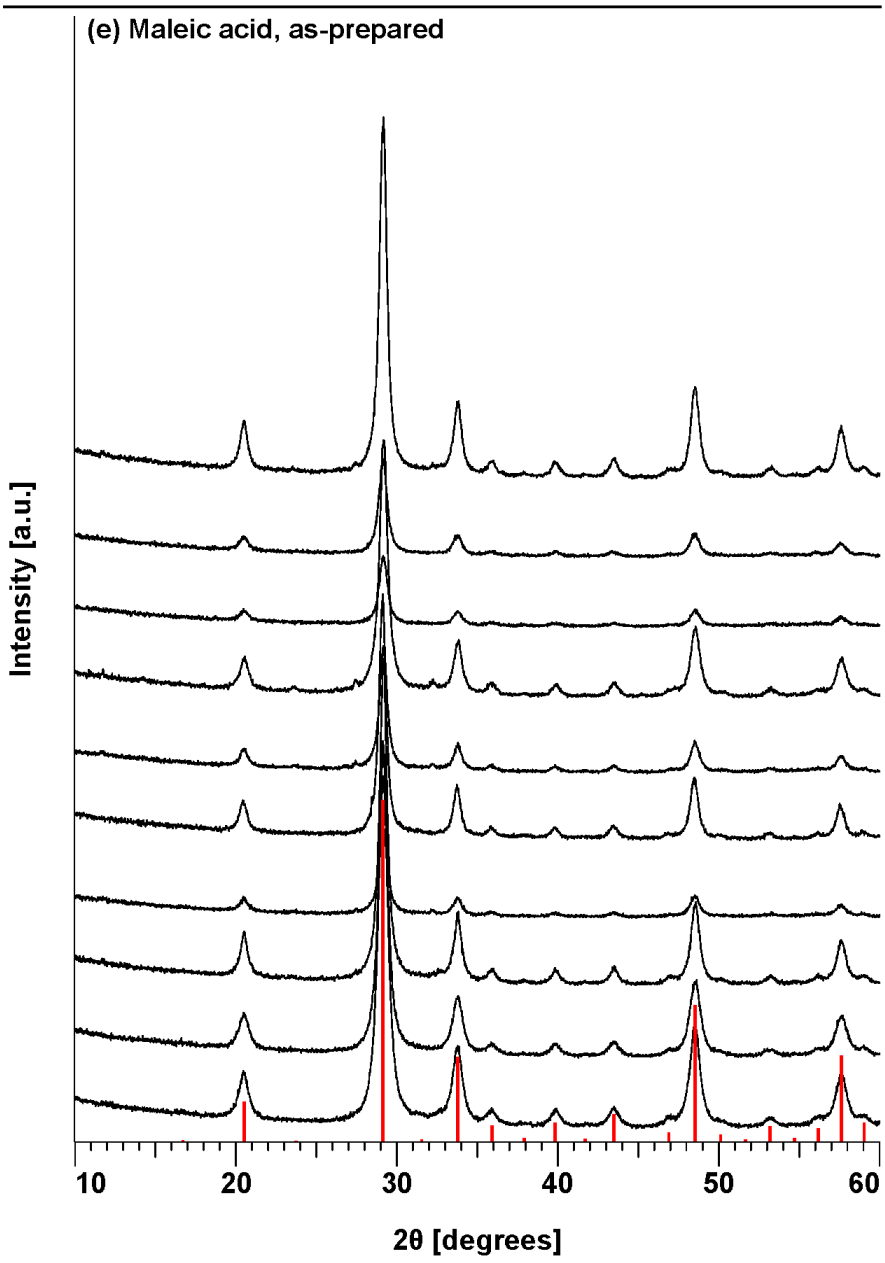

(Fig. 4.2 continues)

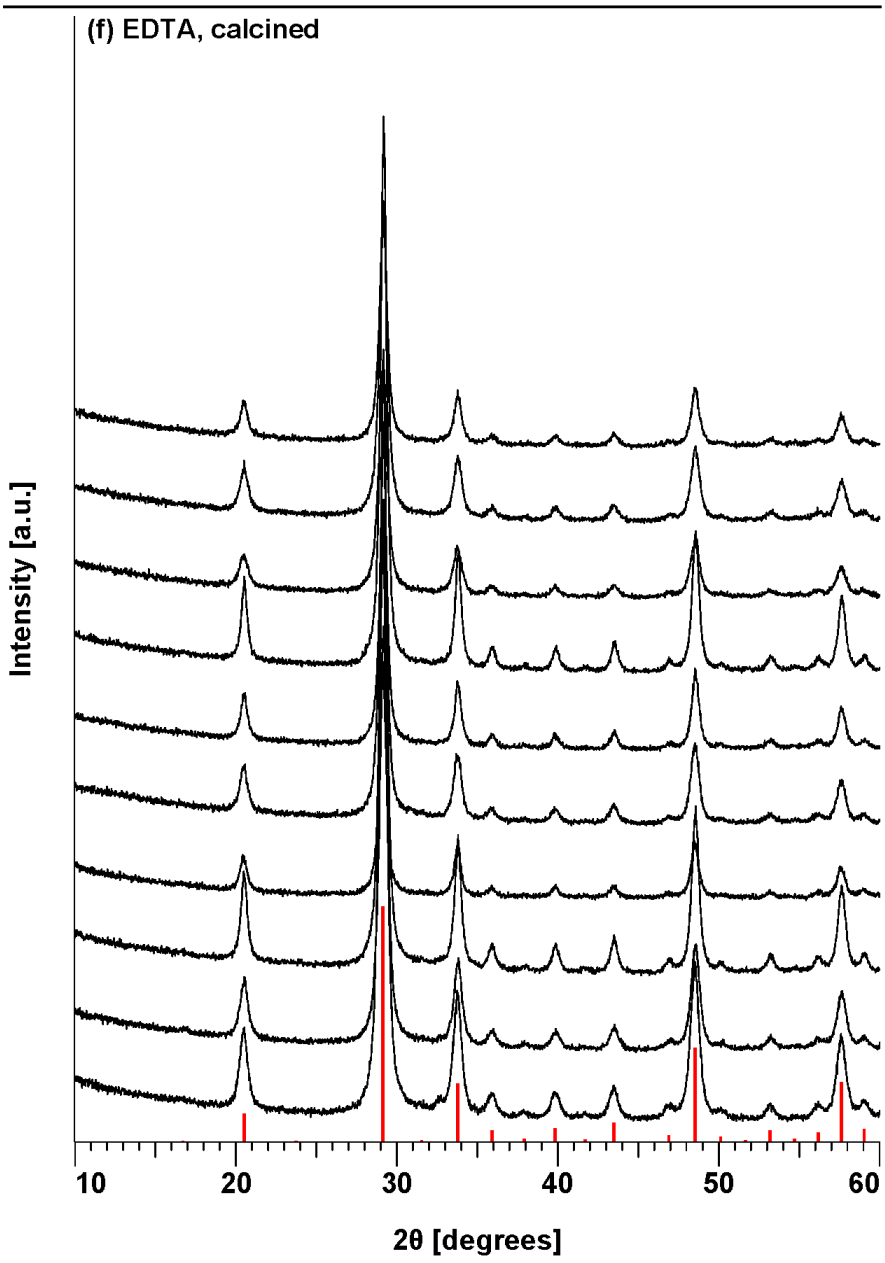

Figure 4.2: *X-ray driffractograms of doped and undoped samples: (a) as-prepared, non-complexed, (b) as-prepared, maleic acid, (c) as-prepared, EDTA, (d) calcined, non-complexed, (e) calcined, maleic acid, (f) calcined, EDTA.*

Table 4.2: *Crystallite sizes of as-prepared and calcined samples calculated by Eq. 3 and crystallite sizes and unit cell parameter of calcined samples estimated by Rietveld refinement and secondary phases*

	Scherrer		Rietveld		Secondary phases	
	As-prepared	Calcined	Calcined			
Sample	***d* [nm]**	***d* [nm]**	***d* [nm]**	**Unit cell length [Å]**	**As-prepared**	**Calcined**
N-75-15	12	15	19	10.603	LSCF	LSCF
N-150-15	(Moist)	16	20	10.612		
N-300-15	11	16	20	10.614		
N-75-30	10	15	20	10.614		
N-75-30-Eu	10	14	18	10.616	Unknown	Unknown
N-150-30	9	15	20	10.615		
N-300-30	9	16	20	10.615		
N-75-40	9	15	20	10.616	Unknown	
N-150-40	9	15	20	10.615	Unknown	
N-300-40	9	14	17	10.617	Unknown	
M-75-15	8	12	16	10.615		
M-150-15	4	11	14	10.614		
M-300-15	13	16	17	10.613		
M-75-30	6	14	17	10.621		$Y_2O_2CO_3$
M-75-30-Eu	8	17	18	10.618		
M-150-30	10	14	16	10.619		$Y_2O_2CO_3$
M-300-30		14	15	10.617	(Amorphous)	$Y_2O_2CO_3$
M-75-40		13	16	10.616	(Amorphous)	
M-150-40		13	16	10.619	(Amorphous)	
M-300-40		15	17	10.614	(Amorphous)	
E-75-15	8	14	17	10.610	Unknown	
E-150-15	8	15	17	10.611		
E-300-15	10	17	21	10.610		

(Table 4.2 continued)

E-75-30		17	17	10.611	(Amorphous)
E-75-30-Eu		14	18	10.614	(Amorphous)
E-150-30	12	18	20	10.611	
E-300-30	19	23	22	10.610	
E-75-40		14	16	10.615	(Amorphous)
E-150-40	8	14	17	10.614	
E-300-40	28	16	18	10.611	

4.4 Scanning electron microscopy

Scanning electron micrographs of all as-prepared and calcined samples are shown in Figs. 4.3–6 and Figs. 4.7–10, respectively. N-150-15, M-150-15 and E-300-15 were too moist to be suited for the SEM. All samples were a mixture of spherical and irregular broken crust-like particles. Samples prepared from complexed precursor solutions had a larger fraction of irregular broken crust-like particles. This morphology did not change during calcination, and no necking could be observed. The spherical particles appeared to be hollow inside, and their crusts were thinner when prepared from solutions containing complexing agent. Average sphere diameter calculated by counting and measuring at least 50 spheres in each micrograph are presented in Table 4.3. The diameters were all in the micrometer range. The smallest particle size was 2.42 µm, obtained for as-prepared N-75-30, and the largest for calcined E-150-15 with 9.35 µm. From these measurements, no clear trends appear, but some tendencies do. The strongest tendency comes from the complexing agents. When other parameters are held constant, precursor solutions complexed with EDTA yielded in most cases the largest particles, while the smallest particles were obtained from non-complexed precursor solutions. In other words, the tendency was EDTA > maleic acid > non-complexed. Size distribution histograms are shown in Figs. A1–A6. The standard deviation in size, σ, varied between 51 and 111 % of the average size of its corresponding sample, with more than half of the samples

being between 60 and 90 %. No parameter varied in this work seemed to have significant effect on the D/σ ratio. When calcined, some samples increased their size, while others decreased theirs. There seems, however, to be a tendency for samples prepared from complexed precursor solutions to decrease rather than increase.

Table 4.3: *Average particle diameter estimated from measurements on SEM micro-graphs.*

	As-prepared		***Calcined***	
Sample	***D***	***σ***	***D***	***σ***
N-75-15	4.25	2.15	4.90	4.62
N-150-15			4.17	3.02
N-300-15	4.78	3.63	4.72	3.02
N-75-30	2.42	1.92	2.46	0.98
N-75-30-Eu	2.88	2.47	2.92	2.99
N-150-30	2.85	1.86	2.58	1.63
N-300-30	3.63	2.72	4.30	3.96
N-75-40	2.61	2.49	2.58	1.46
N-150-40	2.41	2.04	4.08	3.16
N-300-40	2.89	1.53	3.29	2.68
M-75-15	6.07	5.53	4.84	4.03
M-150-15			5.77	3.06
M-300-15	6.31	3.76	6.82	4.86
M-75-30	7.73	8.59	3.97	2.11
M-75-30-Eu	3.82	2.78	3.25	2.02
M-150-30	6.79	5.82	5.27	4.08
M-300-30	3.67	2.24	4.60	3.15
M-75-40	3.64	3.98	3.69	2.40
M-150-40	4.75	3.73	4.14	3.81
M-300-40	6.93	5.98	7.04	3.90

(Table 4.3 continued)

E-75-15	8.43	5.58	7.45	4.16
E-150-15	8.51	4.62	9.35	5.29
E-300-15	8.35	5.56	7.47	5.49
E-75-30	6.37	5.21	4.22	3.65
E-75-30-Eu	6.11	4.78	3.93	2.60
E-150-30	7.10	5.79	7.45	5.97
E-300-30	8.01	4.48	6.06	5.39
E-75-40	3.99	2.79	3.08	3.12
E-150-40	4.92	4.34	4.15	4.33
E-300-40	5.68	4.43	4.87	3.82

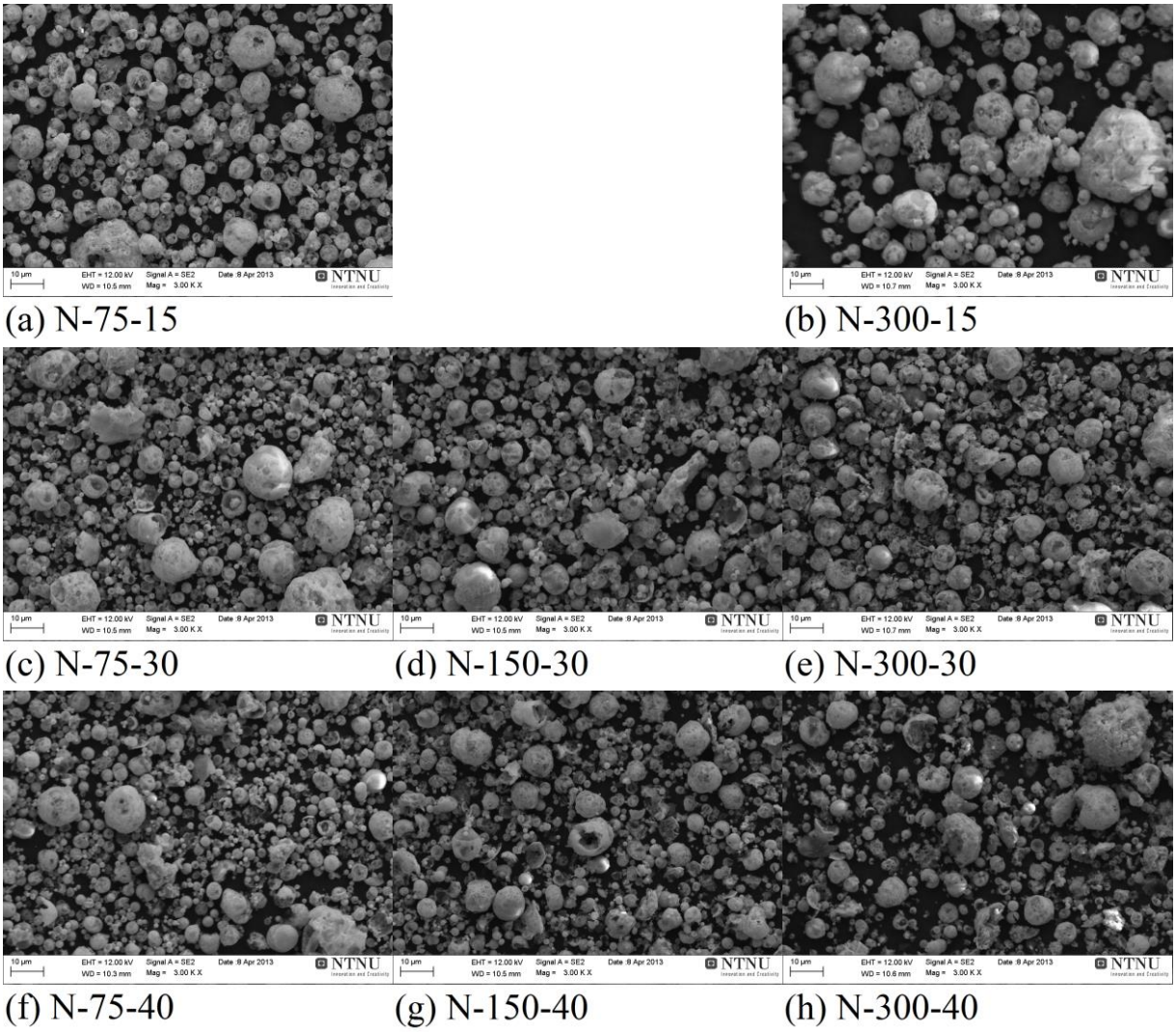

Figure 4.3: *SEM micrographs of as-prepared undoped powders prepared from solution without any complexing agent.*

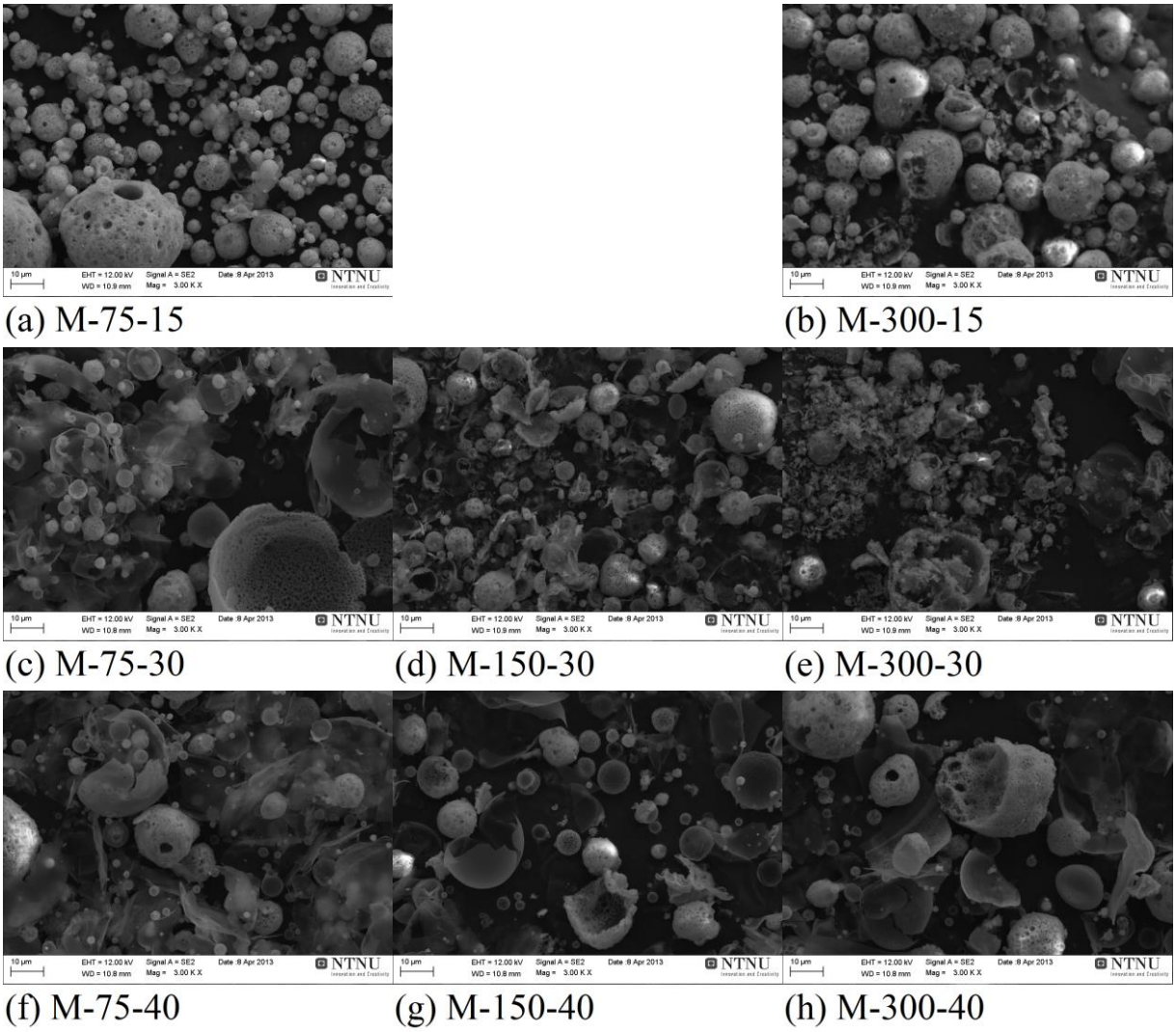

Figure 4.4: *SEM micrographs of as-prepared undoped powders prepared from solution with maleic acid as complexing agent.*

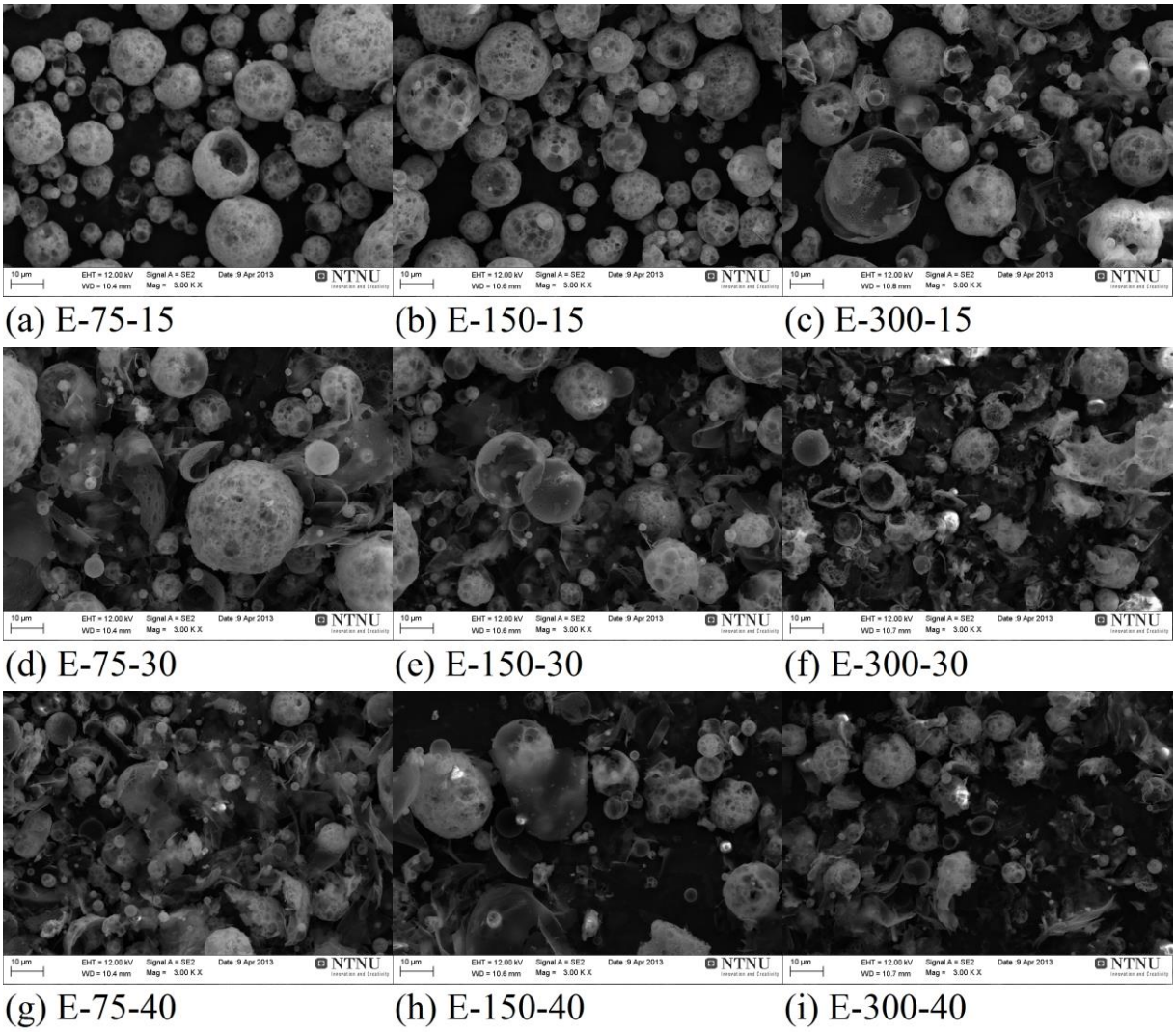

Figure 4.5: *SEM micrographs of as-prepared undoped powders prepared from solution with EDTA as complexing agent.*

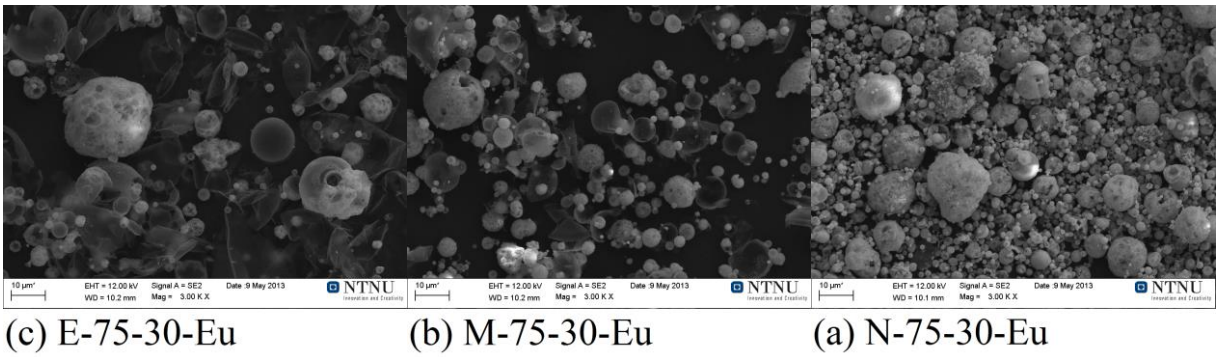

Figure 4.6: *SEM micrographs of as-prepared europium-doped powders.*

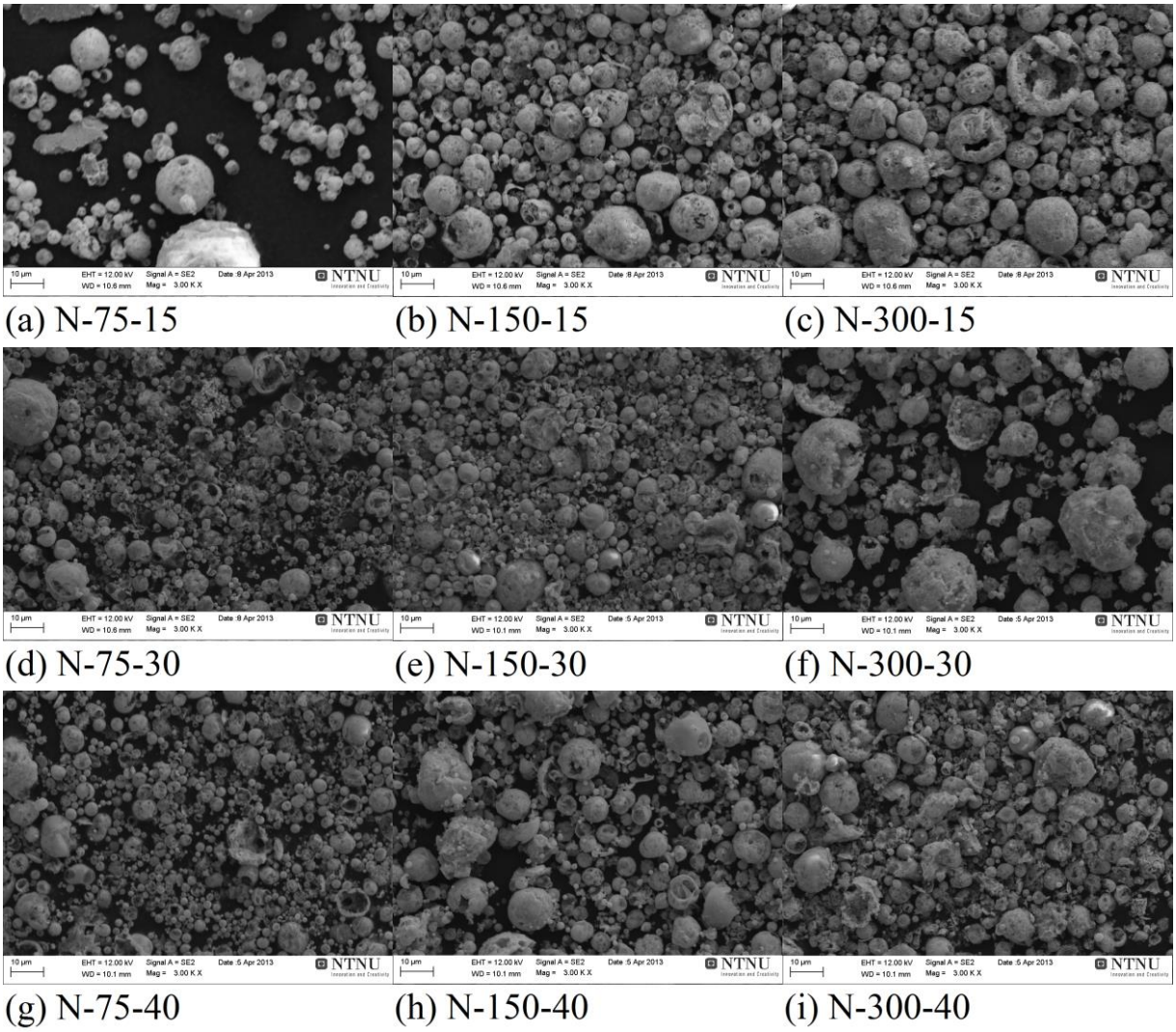

Figure 4.7: *SEM micrographs of undoped powders prepared from solution with without any complexing agent calcined at 600 °C for 2 h.*

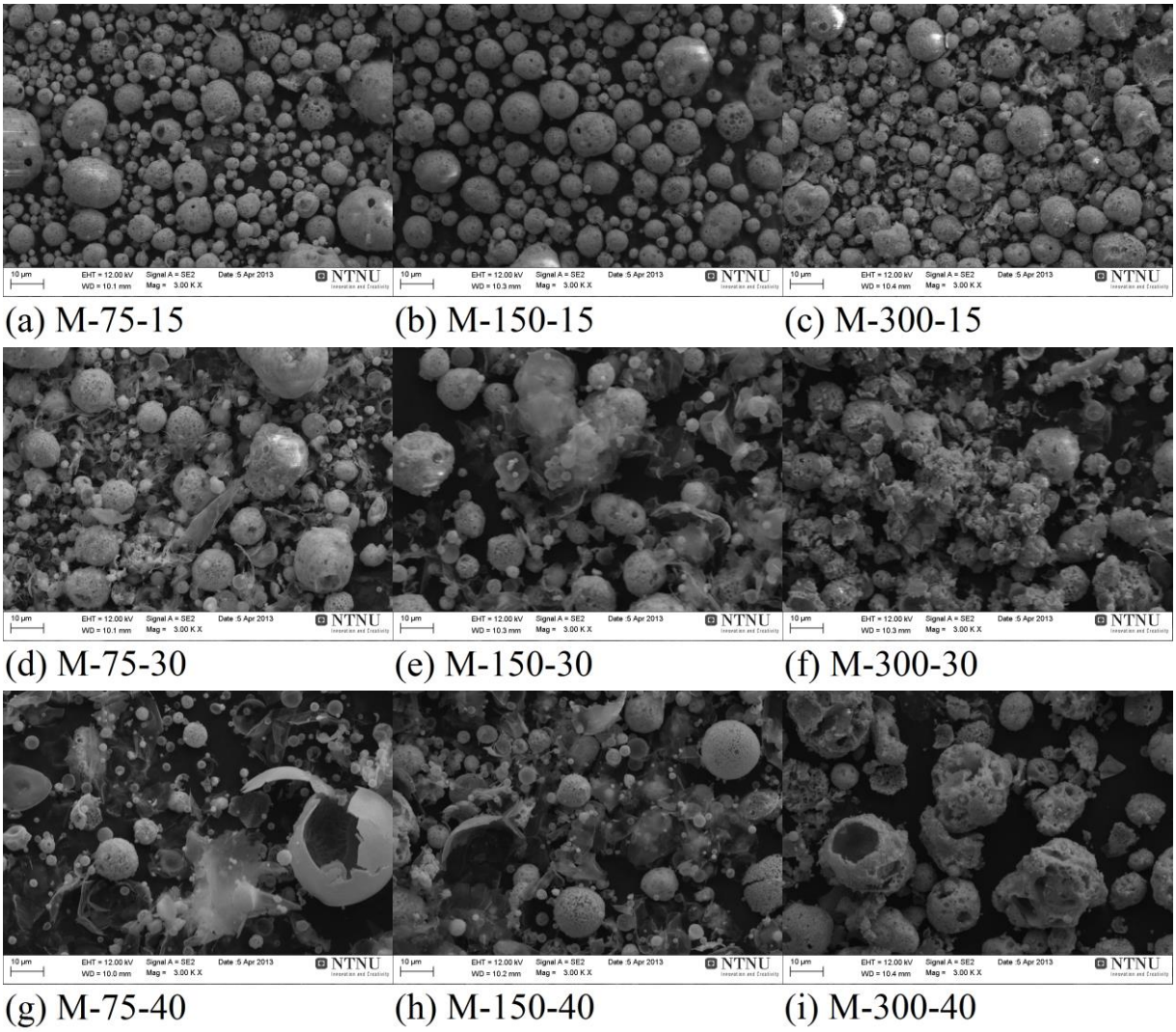

Figure 4.8: *SEM micrographs of undoped powders prepared from solution with maleic acid as complexing agent calcined at 600 °C for 2 h.*

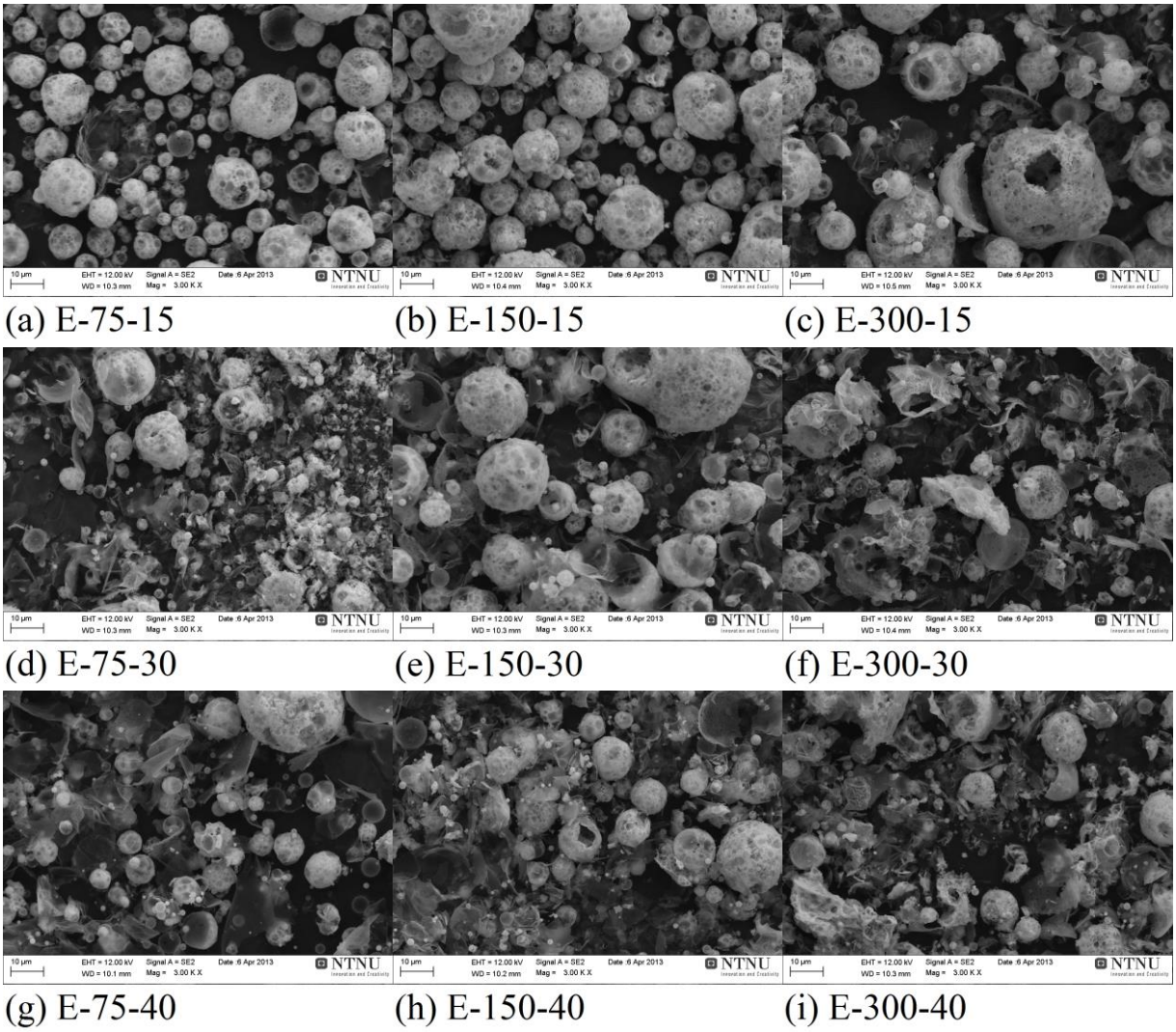

Figure 4.9: *SEM micrographs of undoped powders prepared from solution with EDTA as complexing agent calcined at 600 °C for 2 h.*

4.5 Gas adsorption

Measured specific surface area and average agglomerate size calculated by Eq. 6 of as-prepared and calcined samples are shown in Table 4.4. As-prepared N-150-15, M-150-15 and E-300-15 were too moist to be suited for gas absorption analysis. Gas adsorption measurements were therefore not performed on these samples. Except for M-75-30, all samples had a higher specific surface area when calcined, and the calculated particle size was therefore higher. The specific surface area for these samples increased between 4 and 246 %. M-75-30 had the same surface area before and after calcination. Among the parameters investigated in this work, no single parameter yielded clear trends without exceptions. There seems, however, to be a noticeable effect of complexing agents in the precursor solution. On average, the largest specific surface area, and thus the smallest particles, was obtained with EDTA as complexing agent. Precursor solutions with maleic acid as complexing agent yielded particles with the smallest surface area. When other parameters are held constant, this trend is also seen for a majority of the samples, but not all.

As can by comparing Tables 4.3 and 4.4, the average particle diameters calculated from the SEM micrographs (Figs. 4.3–10) were about two orders of magnitude larger than those calculated by Eq. 6. In turn, these particle sizes are substantially larger than the measured crystallite sizes.

Table 4.4: *Specific surface area, particle size calculated by Eq. 6 and specific surface area increase during calcination of all doped and undoped Y_2O_3 samples.*

Sample	As-prepared		Calcined		
	SA [m^2g^{-1}]	**D [nm]**	**SA [m^2g^{-1}]**	**D [nm]**	**Area increase [%]**
N-75-15	18	66	21	57	17
N-150-15	(Moist)	—	28	43	—
N-300-15	14	85	34	35	143
N-75-30	21	57	30	40	43
N-150-30	20	60	32	37	60
N-300-30	21	57	42	28	100

(Table 4.4 continued)

N-75-40	17	70	40	30	135
N-75-30-Eu	17	70	21	57	24
N-150-40	15	80	46	26	207
N-300-40	13	92	45	27	246
M-75-15	15	80	24	50	60
M-150-15	(Moist)	—	22	54	—
M-300-15	16	75	23	52	44
M-75-30	18	66	18	66	0
M-75-30-Eu	17	70	21	57	24
M-150-30	12	100	17	70	42
M-300-30	22	54	32	37	45
M-75-40	16	75	20	60	25
M-150-40	11	109	18	66	64
M-300-40	10	120	18	66	80
E-75-15	24	50	35	34	46
E-150-15	26	46	34	35	31
E-300-15	(Moist)	—	29	41	—
E-75-30	25	48	34	34	36
E-75-30-Eu	23	52	37	32	61
E-150-30	22	54	31	31	41
E-300-30	26	46	27	27	4
E-75-40	20	60	38	38	90
E-150-40	18	66	36	36	100
E-300-40	10	120	30	30	200

4.6 Infrared spectroscopy

Infrared spectroscopy transmission spectra are shown in Fig. 4.11(a)-(d). There are seven peaks in the spectra that are of interest. The first peak is at approximately 552 cm^{-1} and can be attributed to Y-O stretching. In the samples from complexed precursor solutions (Figs. 4.3 (b) and (c)) it is seen only after calcination. The samples prepared from non-complexed precursor solution it is seen regardless of thermal treatment, indicating that the Y-O bond formed earlier without complexing agents present. The second peak is at around 840 cm^{-1} in both samples prepared from complexed precursor solutions. It could be attributed to the ν2 out-of-plane bending mode of CO_3^{2-} or NO_3^-. This peak is not IR active if the XO_3 (X=C, N) tetrahedra are ideal, and its presence therefore indicates a distortion of the tetrahedral symmetry. If present, this peak causes a split of the ν3 asymmetric stretching vibration frequency. Its intensity increases when the thermal treatment temperature was raised up to 400 °C, but is absent in all calcined samples. The peak at about 1050-1120 cm^{-1} could be assigned to ν1 symmetric stretching vibration of both CO_3^{2-} and NO_3^-. The peaks seen at 1400 and 1540 cm^{-1} corresponds well with the wavenumbers of ν3 asymmetric stretching vibration of both CO_3^{2-} and NO_3^-. This peak could thus be a split peak due to asymmetry of the CO_3^{2-} or NO_3^- tetrahedra. The intensity of the 1400 and 1540 cm^{-1} peaks diminishes progressively as the samples are treated at higher tempereatures, and no great differences between the complexing agents are observed. At 1380 cm^{-1} a very sharp peak is seen. It could be due to adsorption of CO_2 or NO_2. This peak is stronger for the sample prepared from non-complexed precursor solution, and also loses intensity as the heat treatment temperature increases. The broad peak at around 3300-3500 cm^{-1} is assigned to stretching vibration of O-H bonds.

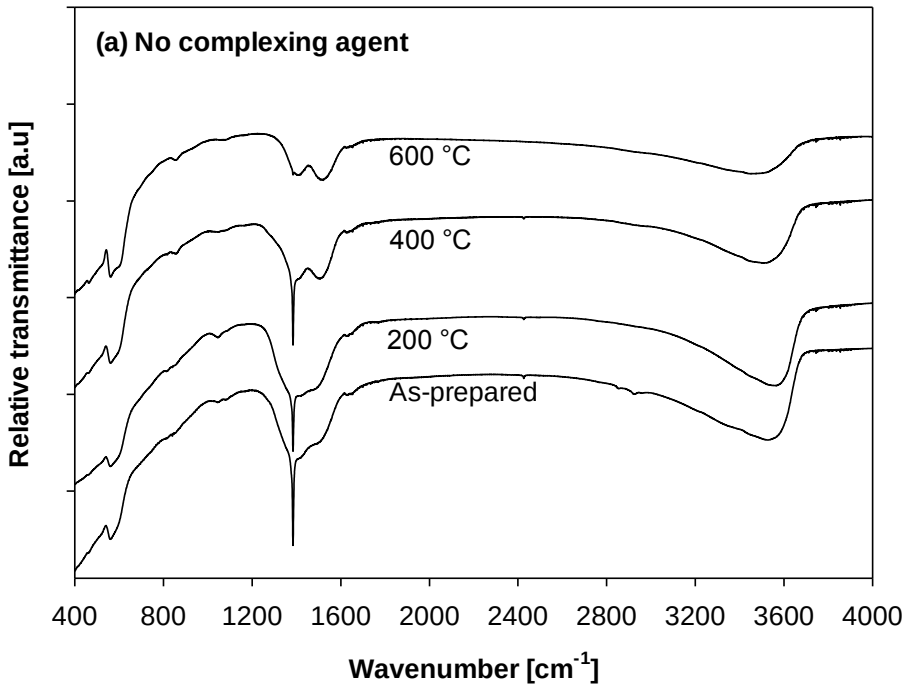

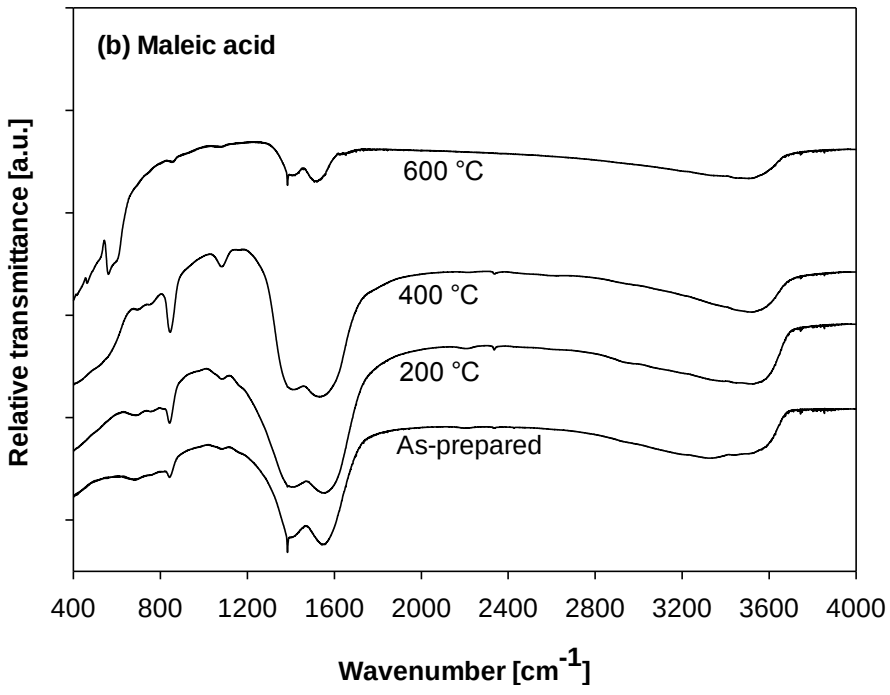

(Fig. 4.11 continues)

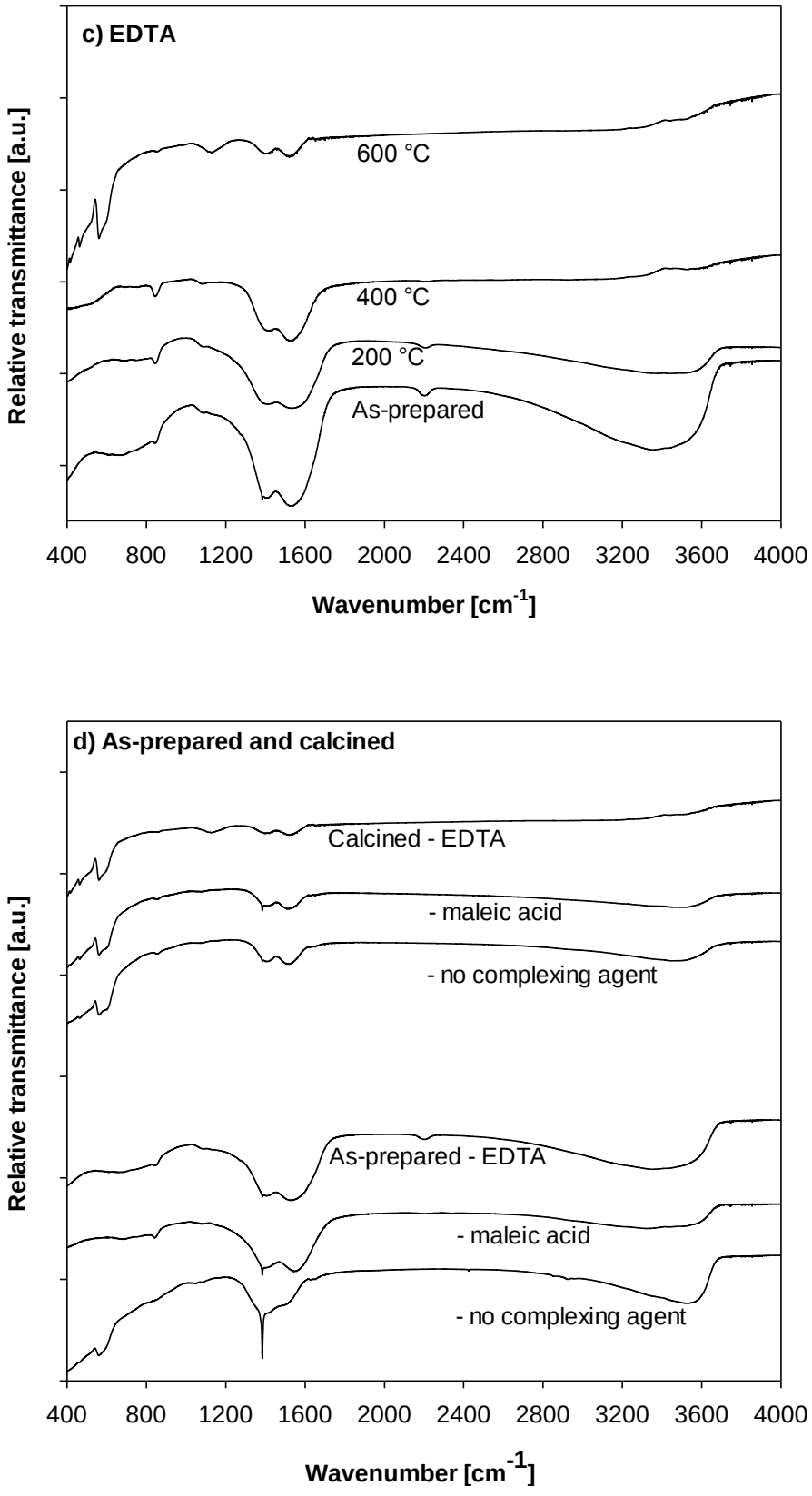

Figure 4.11: *Infrared spectra of Y_2O_3 samples N-75-30, M-75-30 and E-75-30: (a) No complexing agent; (b) maleic acid; (c) EDTA and (d) as-prepared and calcined at 600 °C.*

4.7 Photoluminescence

Emission spectra of the three europium-doped samples after calcination are shown in Fig. 4.12. All samples had maximum intensity at 615 nm, and are in agreement with spectra reported in the literature[44, 53] . N-75-30-Eu had the highest intensity, while the intensities of M-75-30-Eu and E-75-30-Eu were lower by 3 and 26 %, respectively. Fig. 4.13 shows M-75-30-Eu when exposed to ultraviolet light with wavelength 366 nm. This sample had a pale purple glow, while the others did not.

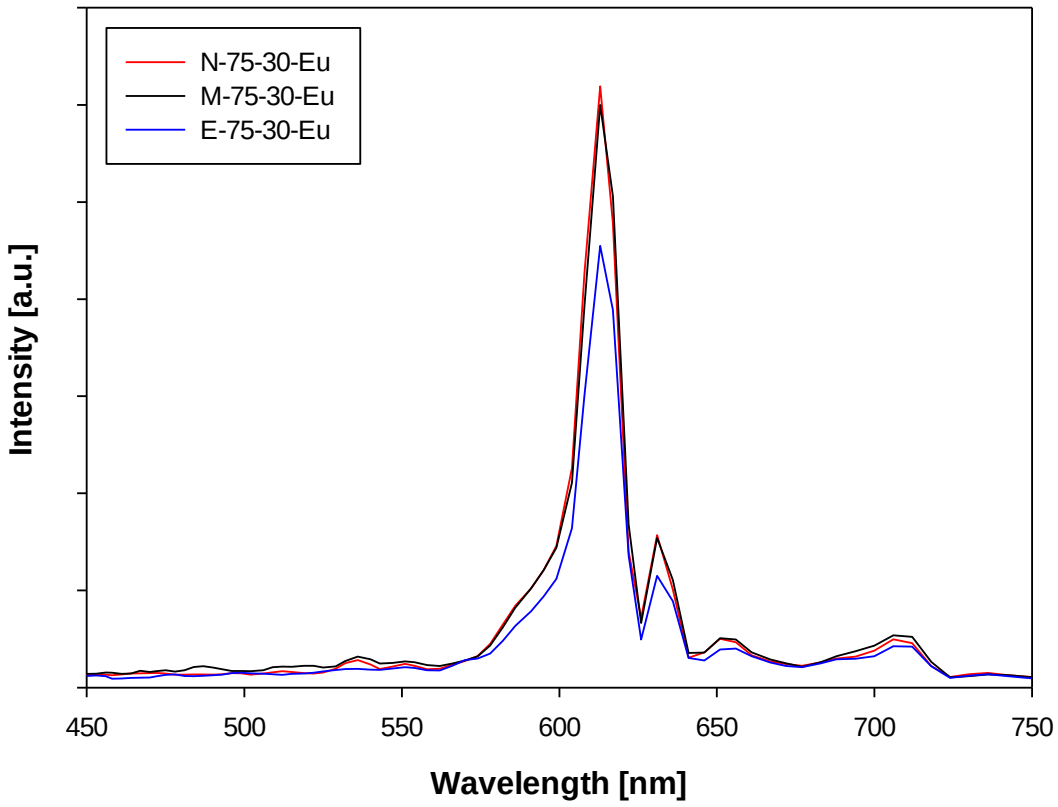

Figure 4.12: *Emission spectra of europium-doped samples after calcination at 600 °C.*

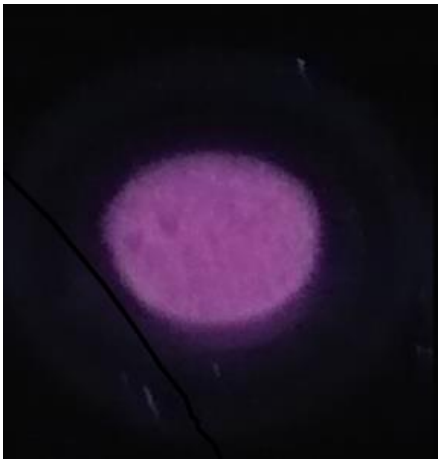

Figure 4.13: *Calcined M-75-30-Eu under exposure to ultraviolet light with wavelength 366 nm.*

5 Discussion

5.1 Moisture

The reason why N-150-15, M-150-15 and E-300-15 were moist or slurry-like when collected from the powder collector may be that the partial pressure of water vapor, P_{H_2O}, inside the furnace was higher compared with the samples prepared with higher carrier gas flow rate. As the gas cooled after leaving the hot-zone the water vapor may have reached saturation and condensed. P_{H_2O} can be estimated based on the following five assumptions:

i. The only gases inside the furnace are air and water vapor
ii. Both water vapor and air are ideal gases
iii. The temperature inside the furnace is T = 1000 °C throughout its volume (i.e. no radial or axial temperature gradient)
iv. Water evaporates immediately after atomization
v. The pressure inside the furnace is P = 1 atm

The flow of water vapor was then calculated by

$$F_v = \frac{F_s R T \rho}{60 \times 10^6 M P} \quad (8)$$

where F_s is the precursor solution feeding rate, R is the universal gas constant and ρ and M are the density and molecular weight of water, respectively. Based on this P_{H_2O} was calculated from the ratio between the vapor flow and the total gas flow (water vapor plus carrier gas):

$$P_{H_2O} = \frac{F_v}{F_v + \frac{1273}{298} F_{cg}} \text{[atm]} \quad (9)$$

The carrier gas flow rate is multiplied by 1273/298 to account for the volume expansion when heating the gas from room temperature to 1000 °C. The calculated values are presented in Table 5.1. As can be seen from Table 5.1, all moist samples were prepared under conditions giving a high P_{H_2O}. The higher partial pressure would cause the dew point of to be higher. At = 0.38, 0.45 and 0.62 atm the dew point is approximately 75, 79 and 87 °C, respectively. It is not unlikely that the temperature near or in the powder collector was close to the dew point of these partial pressures. Therefore it seems reasonable to attribute the moisture of the powder to condensation due to the high P_{H_2O}. Table 5.1 suggests that the partial pressure was highest when the precursor solution feeding rate was 300 mL min^{-1} and the carrier gas flow rate was 15 m^3 h^{-1}. These conditions would therefore be more likely to yield moist samples. N-300-15 and M-300-15 were, however, not moist. This might indicate that the P_{H_2O} was highest under other conditions for these samples, or that the temperature near or close to the powder collector was lower when these samples were produced. If was higher under other conditions than suggested by Table 5.1, it is an indication that the model applied is flawed. If there was a lower temperature during the preparation of these samples, the model could be correct, but not able to accurately predict whether condensation would occur or not.

Table 5.1: Calculated P_{H_2O} inside the furnace as a function of precursor solution feeding rate and carrier gas flow rate. Values for P_{H_2O} are in atm.

F_s [mL min^{-1}]	F_{cg} [m^3 h^{-1}]		
	15	**30**	**40**
75	0.29	0.17	0.13
150	0.45	0.29	0.24
300	0.62	0.45	0.38

5.2 Yield

There may be several reasons for the generally low yield of production. Yield will obviously always be lower than 100 %, but 40–60 % is still a very low value. The most probable reason for this low yield is that the batch size (10 g) was so small that effects of start-up and run-down when switching between batches made significant contributions. Higher yields would therefore be expected for larger batches, where the contributions of such effects would diminish.

5.3 Composition and purity

As shown in the x-ray diffractograms of the calcined samples (Fig. 4.4), the samples were mostly phase pure with only a few samples containing secondary phases. Yttrium oxycarbonate, $Y_2O_2CO_3$, which was found in M-75-30, M-150-30 and M-300-30, forms as reaction intermediate when yttrium carbonate, $Y_2(CO_3)_3$, decomposes and stepwise releases carbon dioxide, CO_2. Yttrium oxycarbonate is therefore the last intermediate before forming yttrium oxide. It is reported to decompose into Y_2O_3 at around 500 °C[55]. This suggests that when sources of carbon, like organic complexing agents, are present in the vicinity of yttrium nitrate, formation of carbonates is favored over formation of the pure oxide at low temperatures. However, many samples were prepared from complexed precursor solutions without the oxycarbonate phase being detected by x-ray diffraction. There may be several reasons for this. One is of course that the phase was not formed in other samples prepared from complexed precursor solutions. This seems unlikely, though, because of the amount of carbonaceous gases that evolve during decomposition of the compexing agents. More probable is it that the oxycarbonate phase indeed did form in other samples as well, but the amounts were so modest that the concentration was below the detection limit of the x-ray diffractometer, which typically is about 1 %. The detection limit increases if the background signal is stronger or there is more noise in the spectrum. The presence of yttrium oxycarbonate is in agreement with what Moen[39] found in his earlier work. The infrared transmission spectra in Fig. 4.3 showed that carbonates were present also in samples were the oxycarbonates were not detected by x-ray diffraction. This further supports that the oxycarbonate phase was present in other samples, but in too low concentrations. Since the oxycarbonate is present after calcination at 600 °C despite its reported lower decomposition temperature, it is evident that kinetics, not thermodynamics, is the reason for its presence.

The unknown secondary phases detected in as-prepared N-75-40, N-150-40, N-300-40 and M-75-15 did not show in the diffractograms of their calcined counterparts. Since no secondary phases were detected in the calcined samples, it is reasonable to assume that the unknown secondary phases were organic and decomposed during calcination. A secondary phase was also detected in N-75-30-Eu, but this phase was still present after calcination. Insufficient cleaning of the apparatus is a likely cause.

The reason why as-prepared M-300-30, M-75-40, M-150-40, M-300-40, E-75-30, E-75-30-Eu and E-75-40 had very low crystallitnity or were amorphous might be related to the evolution of gases during decomposition of precursor and intermediates. The gases may have acted as a barrier for diffusion of yttrium and oxygen.

The infrared transmission spectra also showed the presence of CO_3^{2-} and NO_3^- functional groups, indicating that the calcining at 600 °C for two hours was insufficient for complete decomposition of the precursor and removal of reaction intermediates. Another aspect of the infrared transmission spectra worth noting is the temperature for where the Y-O stretching peak (552 cm^{-1}) becomes apparent. In the sample prepared from non-complexed precursor solution it is present in all spectra, while for those prepared from complexed precursor solution it is present only after calcination. The presence of organic compounds therefore decreased the reaction rate for formation of yttrium oxide, and necessitated thermal treatment at higher temperatures before this bond would form. This is also in good agreement with the color of the samples (Fig. 4.1). Only after calcination did the samples prepared from precursor solution become white, whereas the non-complexed precursor solution yielded white as-prepared powders. The white color is therefore most likely related to the formation of the oxide. Calcination should therefore be performed either at a slightly higher temperature or longer time to remove all carbonates and nitrates.

The smaller unit cell length of N-75-15 could be explained by the LSCF contamination[1] due to insufficient cleaning of the apparatus after the last time the apparatus was used. The cations may have entered the Y_2O_3 lattice and substituted Y^{3+}. In turn this may have distorted the lattice, causing the unit cell to contract.

[1]Recall that LSCF was the composition prepared by the last user of the appratus.

5.4 Size and morphology of crystallites and particles

The SEM micrographs showed that average diameter of the spherical particles increased when the size of the complexing agent ion increased. There are at least three probable reasons for this. First is the diffusivity argument. Complexes formed in solution probably have lower diffusivity than the Y^{3+} and NO^{3-} ions in the non-complexed precursor solution. As a result of this, the concentration profile inside the droplet would have been steeper, and the onset of precipitation would occur after a shorter time, when the droplet radius had not reduced as much. Second is the initial droplet size argument. Complexing agents may have affected the surface tension or viscosity of the precursor solution. A high surface tension or viscosity would make it more difficult to make small droplets, because small droplets would require more energy. Consequently, the initial droplet size after atomization of the precursor solution would be larger. Larger initial droplet size would obviously result in larger particles. Third and last is the solubility argument. If the solubilities of the complexes were lower than the non-complexed precursor they would precipitate after a shorter period in time. Thus, the particle size would be larger. This last argument is, however, unlikely to be correct, since the complexes have higher solubility. Based on the results from this work alone it cannot be concluded with certainty whether the diffusivity argument or the initial droplet size argument is more likely. However, the fact that the crust thickness seemed to have reduced when using complexed precursor solutions might give some indications: If two droplets with initially equal size and concentrations of precursors, but in one of the droplets the precursor diffuses slower than the in the other, precipitation would occur earlier in the slow-diffusion droplet. This would cause a larger particle size in this droplet than in the fast-diffusion droplet. Since the droplets had initially equal size and concentrations of precursor, the fast-diffusion droplet would have a thinner crust than the slow-diffusion droplet. If the droplets instead had initially equal concentrations of precursor, but one were larger than the other, and the diffusivity of the precursor was equal, the situation would be different. Now, the initially large droplet would simply be a magnified copy of the small droplet. There is one factor that strengthens the diffusivity argument and one that weakens the initial droplet size argument. As mentioned in Chapter 4.4, the crusts of the particles prepared from complexed precursor solutions were thinner. This weakens the initial droplet size argument, since larger particles then should have thicker crusts than small particles. In addition, it is reasonable to assume that the diffusivity of the larger and heavier Y-EDTA complex is lower than for the Y-maleic acid complex, which in turn is lower than the non-complexed ions. This strengthens the diffusivity argument, since

low-diffusivity solutes would give a steeper concentration profile. It should be noted that none of the arguments made above exclude the others, and probably all of them contribute to some extent.

The SEM micrographs showed that the fraction of burst crusts was larger when prepared from complexed precursor solutions. This is probably due to evolution of more gases during decomposition of precursor and complexing agents of these samples than those from non-complexed precursor solutions. The larger volume of the gases compared to solids and their flow through the particles can cause particles to rupture more easily. Another plausible explanation is that the particles from the complexed precursor solutions have poorer mechanical strength because of their thinner crusts, and thus are more prone to breaking.

The formation of hollow instead of dense spherical particles can be explained by the model proposed by Jayanthi *et al.[46]*. Applying Eq. 4 with a critical volume fraction 0.16 the critical concentration of yttrium nitrate is found to be 3.6 M. The equilibrium saturation concentration of yttrium nitrate at room temperature is 5.5 M. The percolation criterion is therefore met. When this criterion was met, volume precipitation would give dense particles. It can therefore be concluded that solutes precipitated only on the surface of the droplets.

During calcination some samples decreased their average spherical particle diameter, while others increased theirs. This may be related to two competing processes taking place during calcination. On the one hand, sintering leads to densification of the particles. This will cause the particle diameter to decrease. On the other hand, the particle diameter may increase because of the inflation due to the gases evolving during decomposition of precursors and complexing agents. The gas adsorption data showed that the specific surface area increased for all except one sample. This is a clear indication that the samples sintered during calcination. The particle sizes calculated based on the specific surface area by Eq. 6 are about two orders of magnitude smaller than those calculated by measuring on the SEM micrographs. The absolute values calculated by Eq. 6 are therefore obviously not correct, and should not be trusted. The main reason for the obviously too small particle sizes calculated by Eq. 6 is that the particles do are not monodisperse or all spherical, which are the assumptions for this equation.

The only work described in Chapter 2.3.2 where the exact same powder preparation conditions and calcination program has been used before is Moen's[39] work. The crystallite sizes obtained in this work are in agreement with what he reported. All works that reported

crystallite sizes of calcined samples used either higher calcination temperature, longer calcination time or both. This makes it difficult to compare the results directly, but in all the other works larger crystallite sizes were obtained than in this work. None of the previous works described in Chapter 2.3.2 could demonstrate effect of complexing agent on the crystallite size. The results in this work therefore seem to agree well with these previous works.

Only Marinkovic *et al.[51]* and Moen reported numerical values for the particle size. Marinkovic *et al.* obtained smaller sizes than what is reported in this work. They did not exclude non-spherical particles in their measurements, as opposed to this work, and the temperature of the hot-zone was lower. Moen[39] used data from gas adsorption to estimate the particle diameter, as was done here by Eq. 6. His results agree very well for the samples prepared from precursor solutions without complexing agent and with maleic acid. The sample prepared from precursor solution complexed with EDTA yielded smaller particles in his work than the same conditions did here. The other works reported that the particles were of micrometric size, but did not quantify what their obtained particle sizes were. A direct comparison between this work and other previous works is therefore not possible. All works where precursor solutions were complexed found that addition of complexing agents to the precursor solution yielded thinner crusts or more irregular-shaped particles. Also this is in agreement with the findings of this work, where addition of maleic acid and EDTA to the precursor solution gave a larger fraction of particles with irregular shapes and thin crusts.

5.5 Photoluminescence

The luminescence intensity of the doped samples presented in Fig. 4.17 showed that the sample prepared from precursor solution complexed with EDTA had substantially lower intensity than the two others. This is in agreement with the findings of the previous works described in Chapter 2.3.2. However, it cannot be concluded that it was the EDTA itself that caused this. There are at least three other factors that may have contributed to the lower intensity. Irregular particle morphology decreases the emission intensity because of the larger concentration of surface defects. Therefore, the many burst crusts, where the concentration of surface defects is likely to be higher, could have contributed to the decreased intensity. Since the emission spectra were recorded from only a single point in the samples, inhomogeneous distribution of the europium ions may have caused an apparently lower intensity. Lastly, if

the density of the pellet made from the EDTA sample was lower, it may also have affected the intensity.

Moen[39] claimed that the emission spectrum was altered in the samples he prepared from precursor solution complexed with maleic acid, because of their pale purple glow when exposed to ultraviolet light with 366 nm wavelength. The same phenomenon is seen for M-75-30-Eu, which was prepared and calcined under the same conditions. His claim is, however, not in agreement with the emission spectra recorded in this work. Purple light corresponds to wavelengths approximately between 400 and 450 nm. The emission spectrum in Fig. 4.17 shows no excitation in this region. Moen's[39] claim is therefore most likely incorrect. A more probable explanation of the purple glow is that there was some dispersion in the energy of the light from the lamp, and that some of it was reflected from the surface of the samples. This is likely because the wavelength of the excitation source he used was 366 nm, which is very close to the aforementioned wavelength of purple.

6 Conclusions

This work has focused on preparation of yttrium oxide powder samples by spray pyrolysis. The objective has been to better understand both this preparation method and how chemical and process parameters affect the characteristics of the powders. The parameters investigated in this work were complexing agents and the flow rates of precursor solution and carrier gas. Three of the samples were also doped with 1.5 % europium for investigation of photoluminescence properties.

All samples were a mixture of particles with spherical and irregular shapes small crystallites (14–22 nm after calcination at 600 °C for 2 hours). The spheres were hollow inside and the crusts were thinner when complexing agents were used. Lower mechanical strength and evolution of gases inside the crusts when complexing agents were used were proposed as likely causes. The particles prepared from solution containing complexing agents also had a larger average diameter than those prepared from non-complexed precursor solutions. The increased particle size was attributed to lower diffusivity of complexed precursors. Some of the samples prepared from complexed precursor solutions contained small amounts of yttrium oxycarbonate. A higher calcination temperature is therefore recommended to ensure complete remove of all carbonates.

At low flow rates of carrier gas and high precursor solution feeding rate, the as-prepared powders were moist. At these conditions, the partial pressure of water vapor inside the furnace was high. The moisture was therefore probably due condensation of water vapor after exiting the furnace. Other effects of the flow rates of precursor solution and carrier gas were not observed. This is a great advantage for producers of ceramic materials using spray pyrolysis, as it makes high production rates possible without influencing the powder characteristics.

Photoluminescence performance for the europium-doped samples was lower for the sample prepared from precursor solution complexed with EDTA. Due to the setup of the experiment, it could not be concluded with certainty that it was the EDTA itself that caused the reduced performance.

Although not aimed at in this thesis, some insights into the importance of proper cleaning procedures have been revealed. The presence of foreign secondary phases in the samples first produced after the previous user, should

Together with Moen's[39] previous work, a thorough investigation of the most important parameters that can be varied in spray pyrolysis has now been carried out. A useful overview of the effect of the above mentioned parameters is put forth. Spray pyrolysis stands out as an appropriate industrial-scale preparation method for nanocrystalline oxide materials. Further investigations could for example study the effect of the temperature inside the furnace, look closer into how the yield can be improved or explore a wider range of the parameters already examined.

References

[1] C.R. Ronda, Phosphors for lamps and displays: an applicational view, Journal of Alloys and Compounds, 225 (1995) 534-538.

[2] E. Sambandan, Inorganic Materials Chemistry, 1 ed., iUniverse, New York, 2008.

[3] B.K. Gupta, T.N. Narayanan, S.A. Vithayathil, Y. Lee, S. Koshy, A.L.M. Reddy, A. Saha, V. Shanker, V.N. Singh, B.A. Kaipparettu, A.A. Marti, P.M. Ajayan, Highly Luminescent-Paramagnetic Nanophosphor Probes for In Vitro High-Contrast Imaging of Human Breast Cancer Cells, Small, 8 (2012) 3028-3034.

[4] S.J. Duclos, Scintillator phosphors for medical imaging, Interface-Electrochemical Society, 7 (1998) 34-39.

[5] H. Aizawa, T. Katsumata, S. Komuro, T. Morikawa, H. Ishizawa, E. Toba, Fluorescence thermometer based on the photoluminescence intensity ratio in Tb doped phosphor materials, Sensors and Actuators A: Physical, 126 (2006) 78-82.

[6] R. Nagaishi, T. KIMURA, S.P. SINHA, Luminescence properties of lanthanide (III) ions in concentrated carbonate solution, Molecular Physics, 101 (2003) 1007-1014.

[7] D. Dosev, B. Guo, I.M. Kennedy, Photoluminescence of Eu3+:Y2O3 as an indication of crystal structure and particle size in nanoparticles synthesized by flame spray pyrolysis, Journal of Aerosol Science, 37 (2006) 402-412.

[8] A. Paulraj, P. Natarajan, K. Munnisamy, M.K. Nagoor, K.P. Nattar, B. Abdulrazak, J. Duraisamy, Photoluminescence efficiencies of nanocrystalline versus bulk Y2O3:Eu phosphor-revisited, Journal of the American Ceramic Society, 94 (2011) 1627-1633.

[9] W.-N. Wang, W. Widiyastuti, T. Ogi, I.W. Lenggoro, K. Okuyama, Correlations between Crystallite/Particle Size and Photoluminescence Properties of Submicrometer Phosphors, Chemistry of Materials, 19 (2007) 1723-1730.

[10] K.Y. Jung, C.H. Lee, Y.C. Kang, Effect of surface area and crystallite size on luminescent intensity of Y2O3:Eu phosphor prepared by spray pyrolysis, Materials Letters, 59 (2005) 2451-2456.

[11] Z. Hou, G. Li, H. Lian, J. Lin, One-dimensional luminescent materials derived from the electrospinning process: preparation, characteristics and application, Journal of Materials Chemistry, 22 (2012) 5254-5276.

[12] M.N. Nazarov, Doh Young, New Generation of Europium and Terbium Activated Phosphors, Pan Stanford Publishing Pte. Ltd., Singapore, 2011.

[13] K.A. Wickersheim, R.A. Lefever, Luminescent behavior of the rare earths in yttrium oxide and related hosts, Journal of the Electrochemical Society, 111 (1964) 47-51.

[14] G.A. Hirata, J. McKittrick, M. Avalos-Borja, J.M. Siqueiros, D. Devlin, Physical properties of Y2O3:Eu luminescent films grown by MOCVD and laser ablation, Applied Surface Science, 113/114 (1997) 509-514.

[15] G. Liu, G. Hong, X. Dong, J. Wang, Silica-coated Y2O3:Eu nanoparticles and their luminescence properties, Journal of Luminescence, 126 (2007) 702-706.

[16] S.T. Mukherjee, V. Sudarsan, P.U. Sastry, A.K. Patra, A.K. Tyagi, Annealing effects on the microstructure of combustion synthesized Eu3+ and Tb3+ doped Y2O3 nanoparticles, Journal of Alloys and Compounds, 519 (2012) 9-14.

[17] A.M. Arabi, A. Maghsoudipour, A. Hosseinnia, A.R. Gardeshzadeh, F. Moztarzadeh, Synthesis of Submicron Nanocrystalline Y2O3: Eu Particles via Solvothermal Approach Using Surface Modifiers, Journal of Inorganic and Organometallic Polymers and Materials, 21 (2011) 69-275.

[18] X. Bai, H. Song, L. Yu, L. Yang, Z. Liu, G. Pan, S. Lu, X. Ren, Y. Lei, L. Fan, Luminescent properties of pure cubic phase Y2O3/Eu3+ nanotubes/nanowires prepared by a hydrothermal method, The Journal of Physical Chemistry B, 109 (2005) 15236-15242.

[19] J.Y. Cho, K.-Y. Ko, Y.R. Do, Optical properties of sol–gel derived Y< sub> 2</sub> O< sub> 3</sub>: Eu< sup> 3+</sup> thin-film phosphors for display applications, Thin Solid Films, 515 (2007) 3373-3379.

[20] Q. Pang, J. Shi, Y. Liu, D. Xing, M. Gong, N. Xu, A novel approach for preparation of Y2O3:Eu3+ nanoparticles by microemulsion-microwave heating, Materials Science & Engineering, B: Solid-State Materials for Advanced Technology, B103 (2003) 57-61.

[21] C. Feldmann, J. Merikhi, Synthesis and characterization of rod-like Y2O3 and Y2O3:Eu3+, Journal of Materials Science, 38 (2003) 1731-1735.

[22] X. Zhang, J. Wang, K. Guo, H. Chen, X. Yang, J. Zhao, Synthesis and luminescence properties of Y2O3:Eu with flower-like microstructure, Journal of Alloys and Compounds, 517 (2012) 149-156.

[23] S. Zeng, K. Tang, T. Li, Z. Liang, 3D flower-like Y2O3:Eu3+ nanostructures: Template-free synthesis and its luminescence properties, Journal of Colloid and Interface Science, 316 (2007) 921-929.

[24] H.S. Yoo, H.S. Jang, W.B. Im, J.H. Kang, D.Y. Jeon, Particle size control of a monodisperse spherical Y2O3: Eu3+ phosphor and its photoluminescence properties, Journal of materials research, 22 (2007) 2017-2024.

[25] M.K. Devaraju, S. Yin, T. Sato, Eu3+:Y2O3 Microspheres and Microcubes: A Supercritical Synthesis and Characterization, Inorganic Chemistry, 50 (2011) 4698-4704.

[26] Z. Lu, D. Qian, Y. Tang, Facile synthesis and characterization of sheet-like Y2O3:Eu3+ microcrystals, Journal of Crystal Growth, 276 (2005) 513-518.

[27] S. Major, A. Banerjee, K. Chopra, Highly transparent and conducting indium-doped zinc oxide films by spray pyrolysis, Thin Solid Films, 108 (1983) 333-340.

[28] A.B. Haugen, I. Kumakiri, C. Simon, M.-A. Einarsrud, TiO2, TiO2/Ag and TiO2/Au photocatalysts prepared by spray pyrolysis, Journal of the European Ceramic Society, 31 (2011) 291-298.

[29] N. Mizutani, L. T-Q, Synthesis of spherical Si 3 N 4 powders by spray pyrolysis of polysilazane, Ceram. Trans., 12 (1990) 59-73.

[30] D.A. Lindquist, T.T. Kodas, D.M. Smith, X. Xiu, S.L. Hietala, R.T. Paine, Boron nitride powders formed by aerosol decomposition of poly (borazinylamine) solutions, Journal of the American Ceramic Society, 74 (1991) 3126-3128.

[31] L.S. Čerović, S.K. Milonjić, L.V. Zivković, D.P. Uskoković, Synthesis of Spherical β-Silicon Carbide Particles by Ultrasonic Spray Pyrolysis, Journal of the American Ceramic Society, 79 (1996) 2215-2217.

[32] J.-W. Ko, J. Yoo, Y.-K. Kim, S.J. Chung, S.I. Yoo, Synthesis and characterization of spherical magnesium di-boride nano-powders obtained by spray pyrolysis, Physica C: Superconductivity, 412 (2004) 1194-1197.

[33] J. Joutsensaari, P. Ahonen, U. Tapper, E. Kauppinen, J. Laurila, V.-T. Kuokkala, Generation of nanophase fullerene particles via aerosol routes, Synthetic metals, 77 (1996) 85-88.

[34] J.H. Kim, V.I. Babushok, T.A. Germer, G.W. Mulholland, S.H. Ehrman, Cosolvent-assisted spray pyrolysis for the generation of metal particles, Journal of materials research, 18 (2003) 1614-1622.

[35] J.H. Kim, T.A. Germer, G.W. Mulholland, S.H. Ehrman, Size-Monodisperse Metal Nanoparticles via Hydrogen-Free Spray Pyrolysis, Advanced Materials, 14 (2002) 518-521.

[36] K.Y. Jung, K.H. Han, Densification and photoluminescence improvement of Y 2 O 3 phosphor particles prepared by spray pyrolysis, Electrochemical and solid-state letters, 8 (2005) H17-H20.

[37] Ž. Antić, R. Krsmanović, V. Đorđević, T. Dramićanin, M. Dramićanin, Optical Properties of Y2O3: Eu3+ Red Emitting Phosphor Obtained via Spray Pyrolysis, (2009).

[38] N. Joffin, B. Caillier, A. Garcia, P. Guillot, J. Galy, A. Fernandes, R. Mauricot, J. Dexpert-Ghys, Phosphor powders elaborated by spray-pyrolysis: Characterizations and possible applications, Optical Materials, 28 (2006) 597-601.

[39] R. Moen, Spray Pyrolysis of Phosphor Materials, in: Department of Materials Science and Engineering, Norwegian University of Science and Technology, Trondheim, 2012, pp. 25.

[40] G.L. Messing, S.C. Zhang, G.V. Jayanthi, Ceramic powder synthesis by spray pyrolysis, Journal of the American Ceramic Society, 76 (1993) 2707-2726.

[41] S.J. H, Atmospheric chemistry and physics of air pollution, in, JOHN WILEY, 1986.

[42] C.R. Ronda, Luminescence, Wiley-VCH, 2007.

[43] M.H. Werts, Making sense of lanthanide luminescence, Science progress, 88 (2005) 101-131.

[44] R.S. Withnall, Jack, Handbook of Visual Display Technology, Springer, 2012.

[45] R. Kubrin, W. Bauhofer, Influence of polymeric additives on morphology and performance of Y< sub> 2</sub> O< sub> 3</sub>: Eu phosphor synthesized by flame-assisted spray pyrolysis, Journal of Luminescence, 129 (2009) 1060-1066.

[46] G. Jayanthi, S. Zhang, G.L. Messing, Modeling of solid particle formation during solution aerosol thermolysis: The evaporation stage, Aerosol Science and Technology, 19 (1993) 478-490.

[47] N. Reuge, B. Caussat, N. Joffin, J. Dexpert-ghys, M. Verelst, H. Dexpert, Modeling of spray pyrolysis—why are the synthesized Y2O3 microparticles hollow?, AIChE Journal, 54 (2008) 394-405.

[48] á. Scherrer, Estimation of the size and internal structure of colloidal particles by means of röntgen, Nachr. Ges. Wiss. Göttingen, 2 (1918) 96-100.

[49] H. Rietveld, A profile refinement method for nuclear and magnetic structures, Journal of applied Crystallography, 2 (1969) 65-71.

[50] J.R. Sohn, Y.C. Kang, H.D. Park, Morphological control of Y_2O_3:Eu phosphor particles by adding polymeric precursors in spray pyrolysis, Japanese Journal of Applied Physics, Part 1: Regular Papers, Short Notes & Review Papers, 41 (2002) 3006-3009.

[51] K. Marinkovic, L. Mancic, L. Gomez, M.E. Rabanal, M. Dramicanin, O. Milosevic, Photoluminescent properties of nanostructured Y_2O_3: Eu^{3+} powders obtained through aerosol synthesis, Optical materials, 32 (2010) 1606-1611.

[52] H. Roh, Y. Kang, H. Park, S. Park, Y2O3: Eu phosphor particles prepared by spray pyrolysis from a solution containing citric acid and polyethylene glycol, Applied Physics A, 76 (2003) 241-245.

[53] H.Y.L. Koo, Sang Ho; Ko, Da Rae; Kang, Yun Chan, Nano-sized Y_2O_3:Eu phosphor powders prepared by spray pyrolysis from spray solution with ethylenediaminetetraacetic acid, citric acid and boric acid, Journal of Ceramic Processing Research, 11 (2010) 4.

[54] R. Jagannathan, T. Kutty, M. Kottaisamy, P. Jeyagopal, Defects induced enhancement of Eu3+ Emission in yttria (Y2O3: Eu3+), Japanese Journal of Applied Physics-Part 1 Regular Papers and Short Notes, 33 (1994) 6207-6212.

[55] N. Imanaka, T. Masui, Y. Mayama, K. Koyabu, Synthesis of crystalline yttrium oxycarbonate in a single phase, Journal of Solid State Chemistry, 178 (2005) 3601-3603.

Appendix A

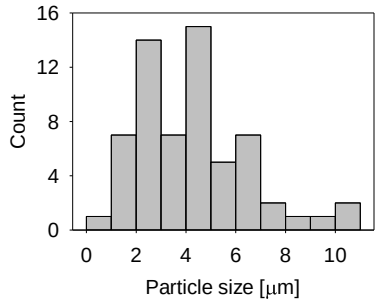

(a) N-75-15

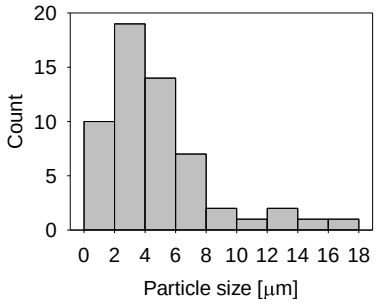

(b) N-300-15

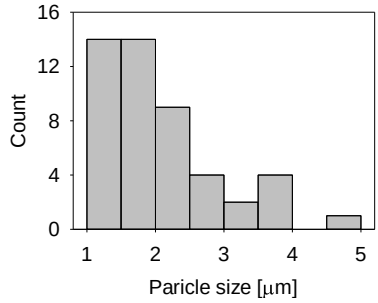

(c) N-75-30

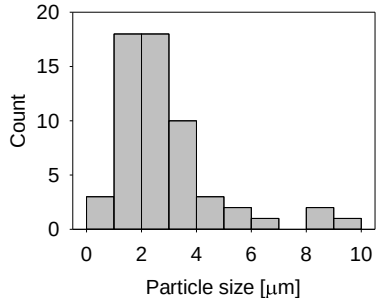

(d) N-150-30

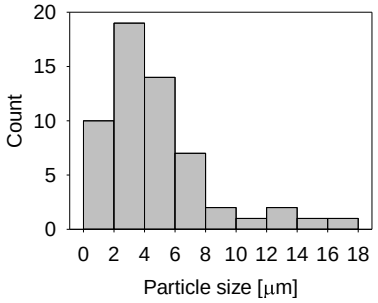

(e) N-300-30

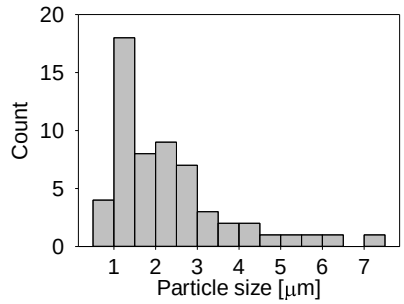

(f) N-75-40

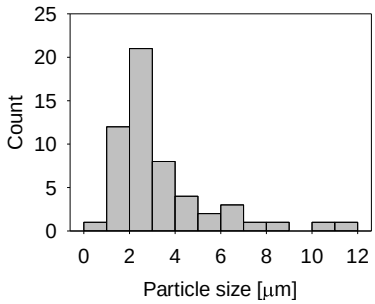

(g) N-150-40

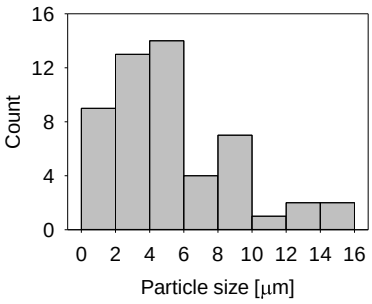

(h) N-300-40

Figure A1: *Particle size distribution histograms of as-prepared samples prepared from non-complexed precursor solution.*

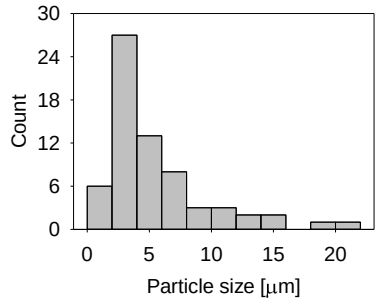

(a) M-75-15

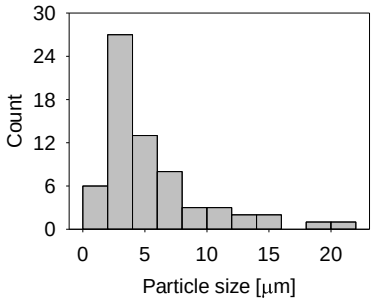

(b) M-300-15

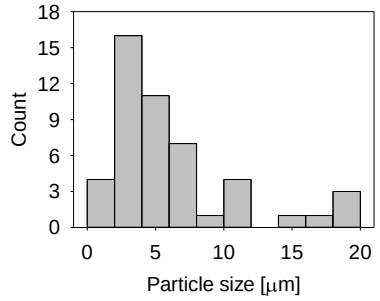

(c) M-75-30

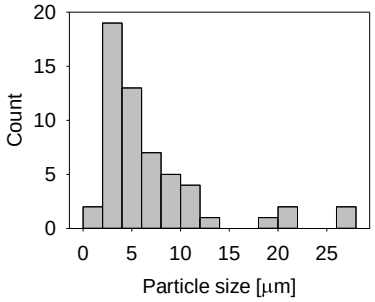

(d) M-150-30

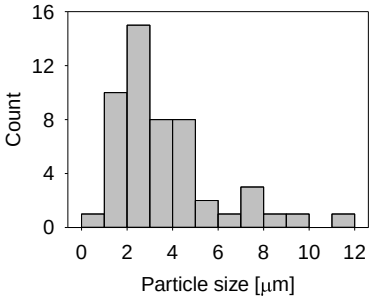

(e) M-300-30

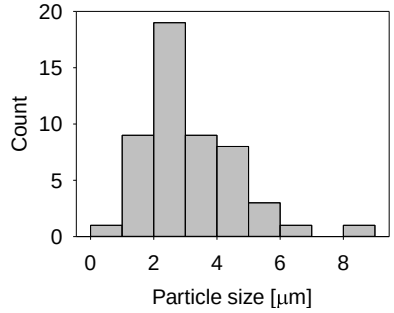

(f) M-75-40

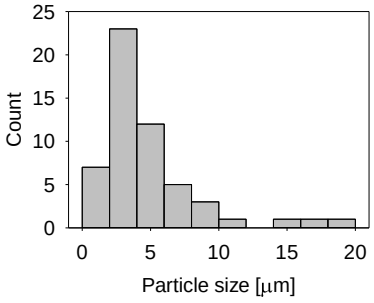

(g) M-150-40

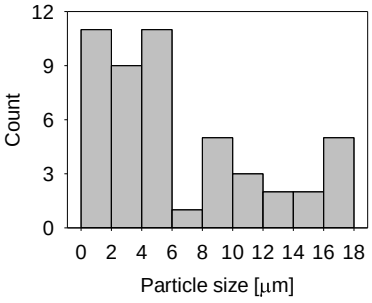

(h) M-300-40

Figure A2: *Particle size distribution histograms of as-prepared samples prepared from precursor solution complexed with maleic acid.*

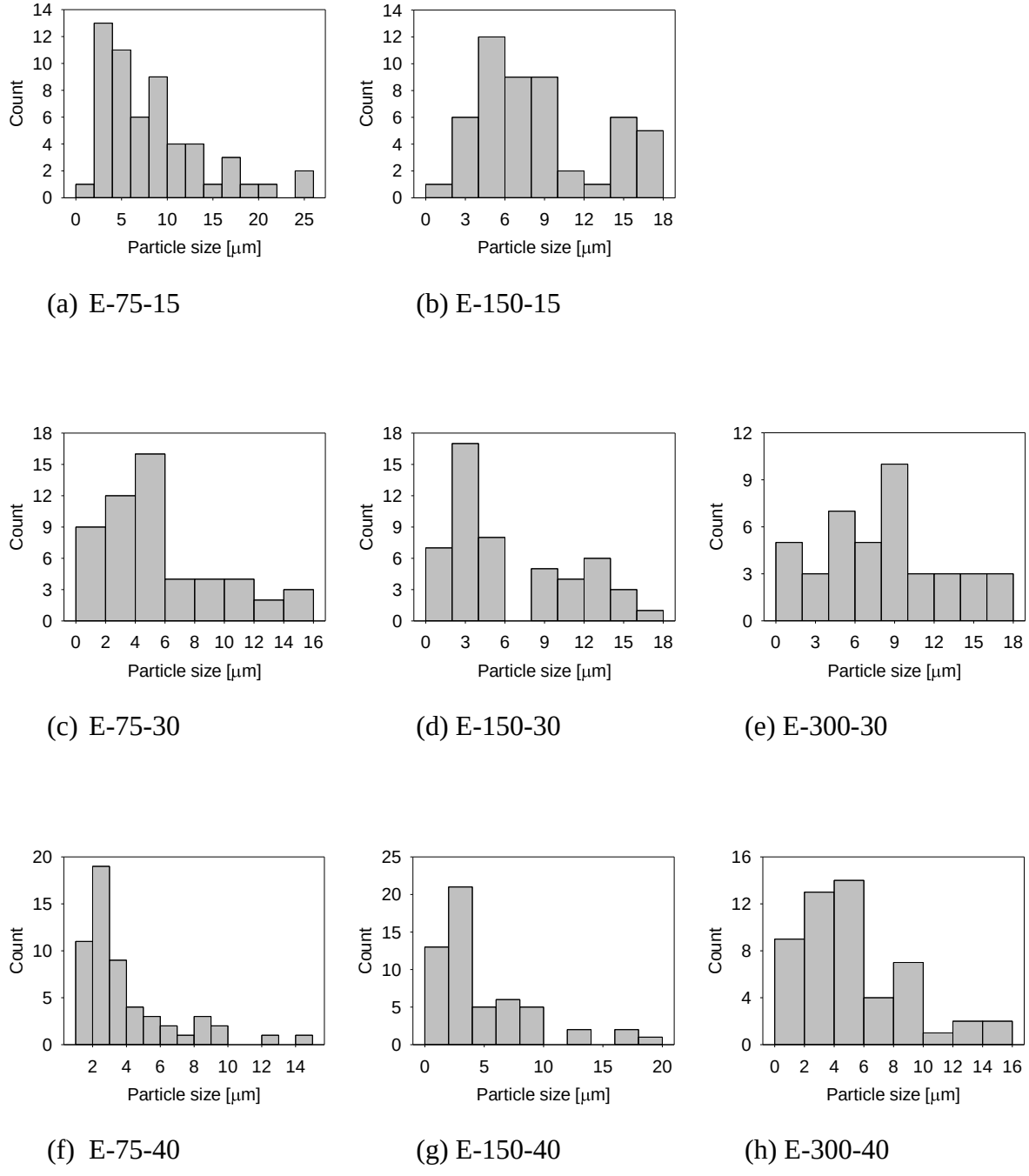

Figure A3: *Particle size distribution histograms of as-prepared samples prepared from precursor solution complexed with EDTA.*

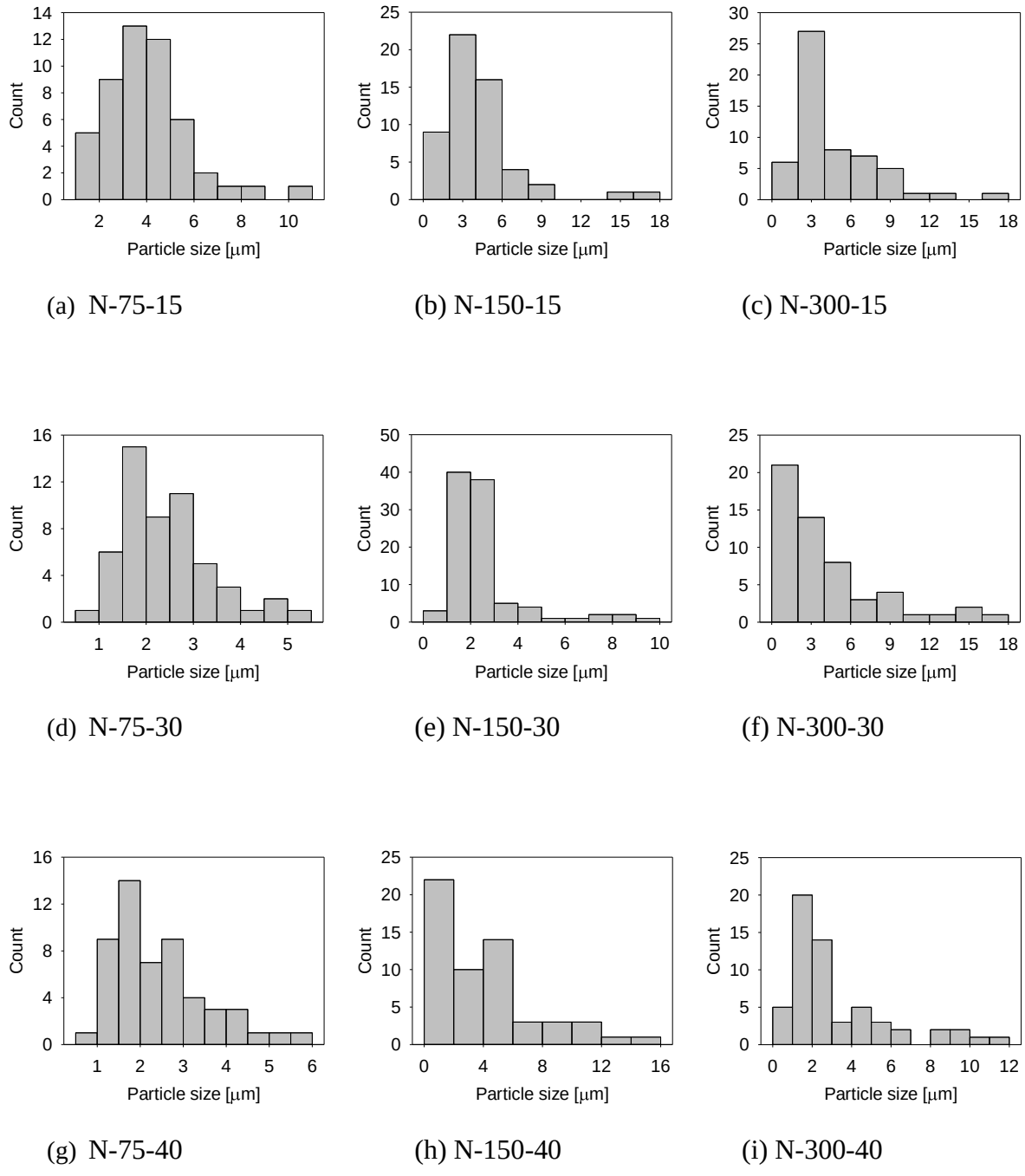

Figure A4: *Particle size distribution histograms of calcined samples prepared from non-complexed precursor solution.*

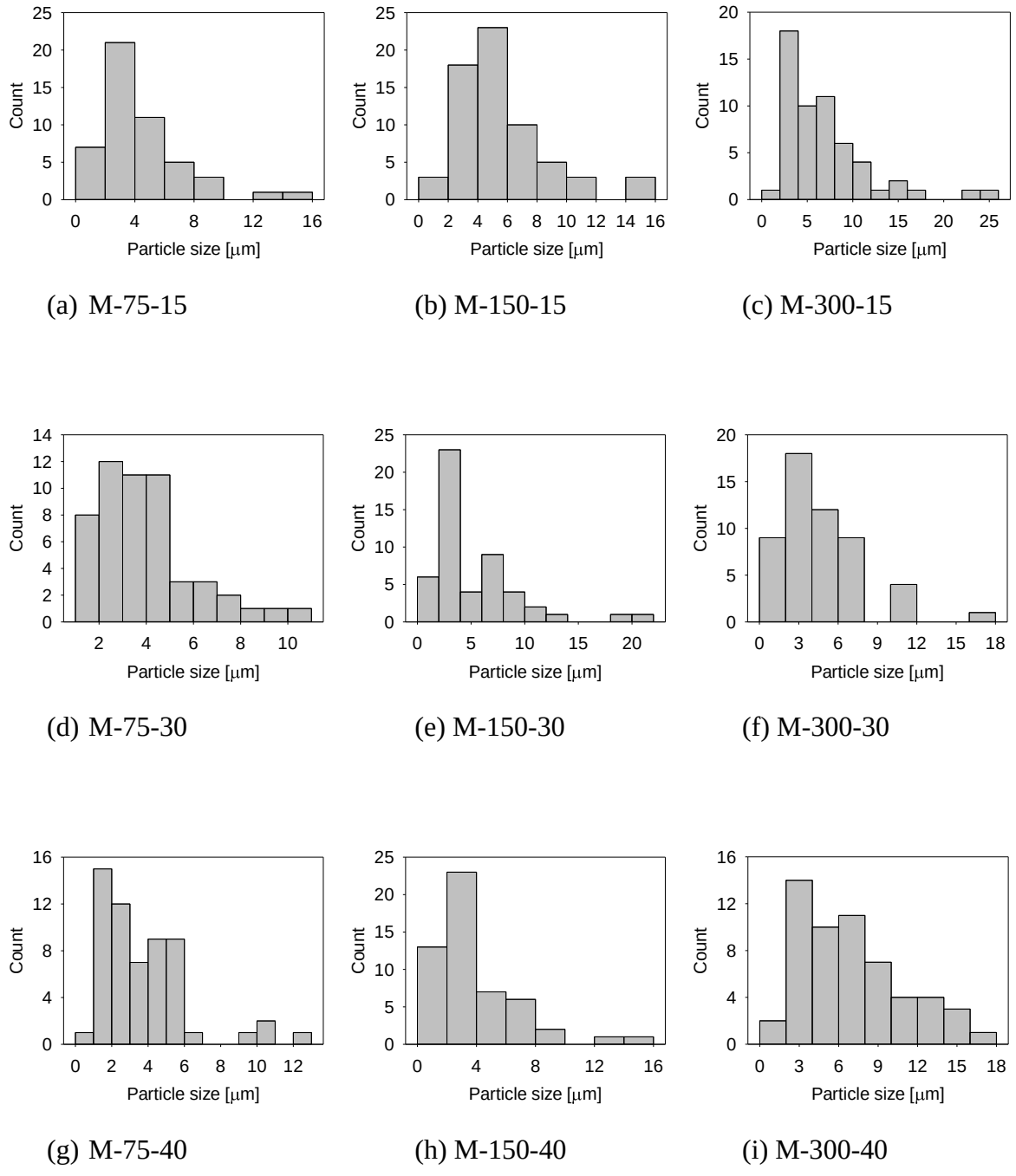

Figure A5: Particle size distribution histograms of calcined samples prepared from precursor solution complexed with maleic acid.

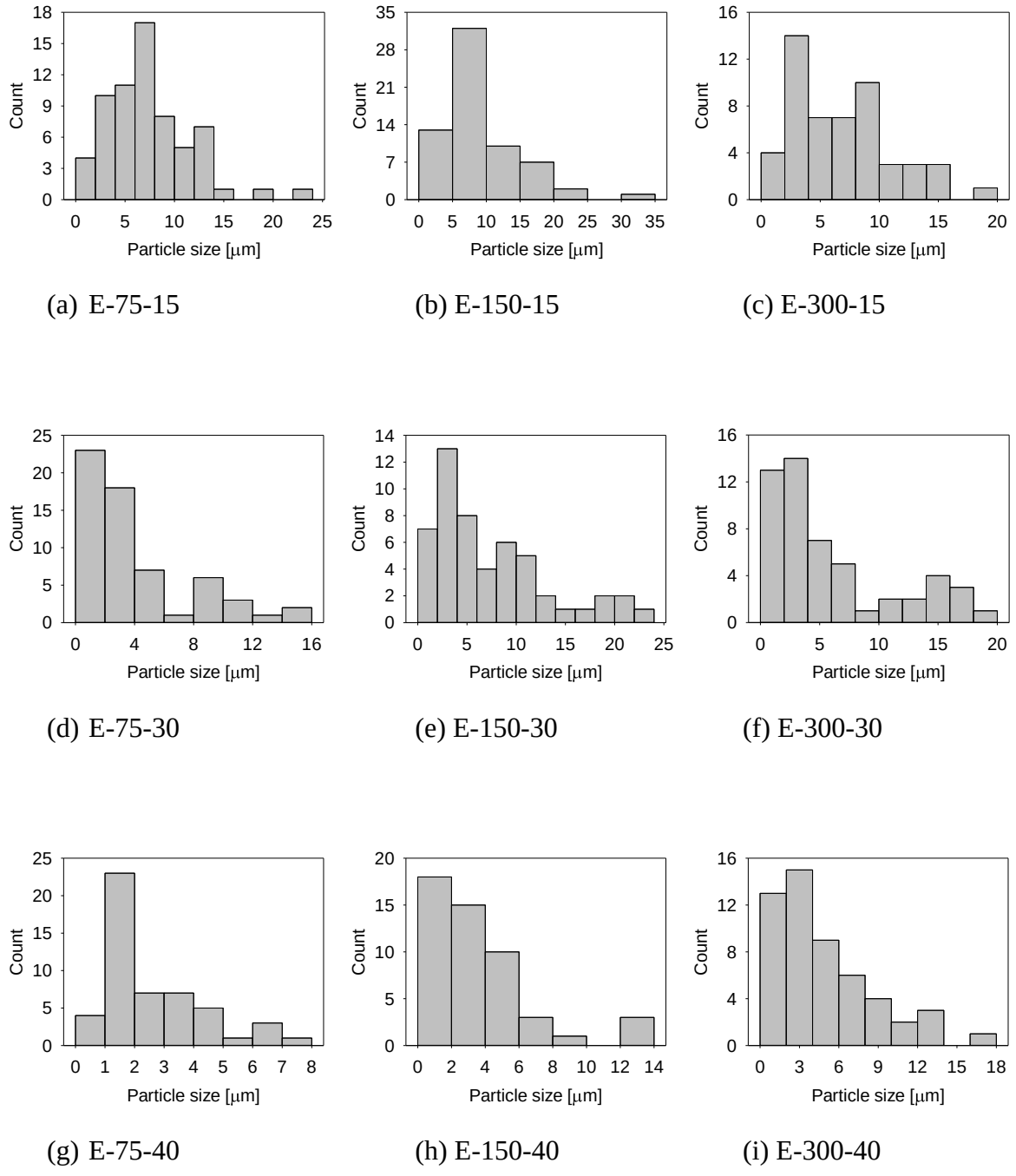

Figure A6: *Size distribution histograms of calcined samples prepared from precursor solution complexed with EDTA.*